CRYSTAL ENGINEERING IN ANTISOLVENT CRYSTALLIZATION OF NEODYMIUM SULFATE

Author: Jonathan Sibanda

Supervisor: Prof. Alison Emslie Lewis

Co-supervisor: Mr. Jemitias Chivavava

Dissertation submitted in fulfillment of the academic requirements for the degree of Master of Science in Chemical Engineering

Department of Chemical Engineering

Faculty of Engineering and the Built Environment

University of Cape Town

Private Bag X3, Rondebosch 7701

Cape Town, South Africa

www.crystal.uct.ac.za

2023

Declaration

I know the meaning of plagiarism and declare that all the work in the document, save for that which is appropriately acknowledged, is my own. This dissertation has been submitted to the Turnitin module, and I confirm that my supervisor has seen my report and any concerns revealed by such have been resolved with my supervisor.

Signed by candidate

Jonathan Sibanda

Acknowledgments

I want to thank my supervisors Professor Alison E Lewis and Mr. Jemitias Chivavava for their guidance and assistance in the completion of the project. Thank you so much for allowing me to go through this journey. Your efforts are sincerely appreciated.

A huge thank you to Miranda Waldron of the Electron Microscope Unit and colleagues in the analytical laboratory of the Chemical Engineering department at the University of Cape Town for all their patience and work.

I would want to appreciate Nikita Bam for all the administrative work she did. You are a star!!! To all the CPU Research Unit students you are appreciated for the support and suggestions during the seminars and the PG sessions.

Special mention goes to my wife, thank you for the prayers and the moral support during the trying times. To my mum and siblings, you are all shining stars. This is all for you.
To GOD be the glory!

Abstract

Antisolvent crystallization is a separation technology that separates a solute from the solvent by the addition of another solvent, in which the solute is sparingly soluble. High yields are achieved by using higher antisolvent-to-solvent ratios, but this generates higher supersaturation, which causes excessive nucleation. This results in the production of smaller or finer particles, which are difficult to handle in downstream processes such as drying and filtration.

Therefore, this study aimed at investigating the effect of varying the organic (antisolvent)-to-aqueous ratio and seed loading on the yield, particle size distribution, and morphology of neodymium sulfate octahydrate product, during its recovery from an aqueous leach solution using antisolvent crystallization. A batch crystallizer was used for the experiments, while ethanol was used as the antisolvent. Neodymium sulfate octahydrate [$Nd_2(SO_4)_3.8H_2O$] seeds obtained from antisolvent crystallization at a lower organic-to-aqueous ratio of 0.4 were used to investigate the effect of seed loading. The crystals exhibited a plate-like morphology, with the plates becoming thinner, rounded, and layered at higher organic-to-aqueous ratios. This was attributed to enhanced physical interactions between the ethanol and the growing crystals, which possibly caused the ethanol to be adsorbed onto the crystalline surfaces, thereby inhibiting growth from one plane to another.

The final particle size distribution curves shifted showing an increase in the particle sizes as the organic-to-aqueous ratio was increased from 0.8 to 1.4. The mean particle size increased from 106.1µm at an organic-to-aqueous ratio of 0.8 to 141.4 µm at an organic-to-aqueous ratio of 1.4. This was attributed to the agglomeration of smaller or fine particles that formed at high supersaturation into bigger particle sizes. The total number of particles decreased while the total volume increased as the organic-to-aqueous increased from 0.8 to 1.4. As the organic-to-aqueous ratio increased from 0.8 to 1.4, the final product yield increased from 44% to 90%. The increase in yield was attributed to the increased interaction of ethanol molecules with the solvent molecules, which reduced the solubility of neodymium sulfate.

Increasing the seed loading above the critical seed loading of 2.98% to 20% resulted in smaller final particle sizes of 101.5 µm compared with 165.8 µm obtained when the system was not seeded. These smaller sizes obtained at seed loadings above the critical seed loading had

narrow particle size distributions. The span of the particle size distribution for the unseeded case was 1.54 while for PSDs obtained at seed loadings above the critical seed loading was less than 1.30. Seeding improved the filtration performance by 47%. This was due to the narrow particle size distribution and improved crystal morphology.

It is recommended that to obtain higher yields and particles with unimodal particle size distribution, higher organic-to-aqueous ratios above 1.2 be used, and seeding be conducted at seeding loadings above the critical seed loading. In addition, if crystals of well-defined or faceted morphology are required it will be reasonable to use a lower organic-to-aqueous ratio such as 0.6 to 0.8 at batch times greater than 2.5 h. The filterability of neodymium sulfate at higher organic-to-aqueous ratios needs to be investigated for future studies.

Journal publication

Sibanda, J., Chivavava, J. & Lewis, A.E. 2022. Crystal Engineering in Antisolvent Crystallization of Rare Earth Elements (REEs). Minerals. 12(12):1554. Available: https://www.mdpi.com/2075-163X/12/12/1554.

Table of contents

List of figures

List of tables

Nomenclature

A	Preexponential factor (nuclei/s)
A_T	Total surface area (m^2m^{-3})
C	Concentration of species I ($molm^{-3}$)
CSD	Crystal size distribution
G	Gibbs free energy ($Jmol^{-1}$)
G'	Crystal growth rate (ms^{-1})
J	Nucleation rate (m^3s^{-1})
k	Boltzmann constant (JK^{-1})
k_a	Surface shape factor (-)
K_{SP}	Solubility product ($kmolm^{-3}$)
K_v	Volume shape factor (-)
L	Crystal size (μm)
L_p	Product crystal size (m)
L_S	Seed mean size (m)
M_T	Total mass (kgm^{-3})
$n\ (L)$	Population density (#/m^3 slurry)
N	Number of particles (-)
N_T	Total number of particles ($\#m^{-3}$)
PSD	Particle size distribution
r	Radius of nucleus (m)
r_C	Critical size of nucleus (m)
REE	Rare Earth Elements
S	Supersaturation (-)
S_a	Surface area (m^2)
SEM	Scanning Electron Microscope
T	Temperature (K)
t_g	Growth time (s)
t_n	Nucleation time (s)
t_r	Relaxation time (s)
V_T	Total volume (m^3m^{-3})

W_S	Seed mass (kg)
W_{th}	Theoretical mass of solute (kg)
v	Molecular volume ($m^3molecule^{-1}$)

Greek symbols

μ	Chemical potential ($Jolmol^{-1}$)
$f(\phi)$	Correction factor (-)
$G_{surface}$	Gibb's free energy between the surface of the particle and the bulk ($Jmol^{-1}$)
G_{volume}	Gibb's free energy between a very large particle and the solute in solution ($Jmol^{-1}$)
ΔG	Gibb's free energy ($Jmol^{-1}$)
θ	Contact angle (^{O})
v_i	Units of species i
Π	pi (-)
γ	Activity coefficient (-)
σ	Interfacial tension (Jm^{-2})

1 Introduction

1.1 Background

Rare earth elements (REEs) consist of 15 lanthanides, from lanthanum (La) to lutetium (Lu), including yttrium (Y) and scandium (Sc) (IUPAC, 1990). REEs such as neodymium (Nd), praseodymium (Pr), and dysprosium (Dy) are used in applications, such as hybrid electric vehicles, magnets for wind turbines, and fuel cells (Alonso et al., 2012; Alves Dias et al., 2020; Lucas et al., 2014; Yoon et al., 2014). The use of REEs in these applications has significantly increased their demand. Deposits of these REEs are found in many places around the globe but their chemical properties make it difficult to separate them from their ores.

There has been an impetus to develop strategies and ways of recycling REEs due to concerns about the future availability of these elements. One such strategy is to recover REEs from spent nickel metal hydride (NiMH) batteries. As part of the circular economy, efficient recycling of REEs contributes to the goals of sustainability by focusing on waste reduction in the extraction of REEs. As of 2016, the production of NiMH batteries was one billion cells per year due to their use in HEV (Gras, 2018), which therefore presents a major source for recycling REEs at the end of life of the NiMH batteries. To recover the REEs from the NiMH battery, the battery is dismantled, and the anode material is leached using a strong acid. The residue is then separated from the leach liquor using filtration (Korkmaz et al., 2020). Crystallization and precipitation methods have been employed to recover the REEs from the leach solution.

Antisolvent crystallization is a potentially novel crystallization method that could be used for recovery. It involves the addition of a solvent in which the solute is sparingly soluble to induce its crystallization or precipitation (Genck, 2010). Increasing the amount of the antisolvent helps in decreasing the solubility of the solute, resulting in a higher yield. However, increasing the amount of antisolvent results in increased molecules interacting with the aqueous phase (Kumar et al., 2014; Norouzi et al., 2020). This has the potential to increase the degree of supersaturation in the crystallizer, resulting in excessive nucleation and smaller final particle sizes (Kakran et al., 2012; Raj & Kurup, 2016).

In the recovery of scandium using antisolvent crystallization, Peters et al. (2019) found that using higher quantities of the antisolvent produced smaller crystals of ammonium scandium hexafluoride. This was attributed to a high degree of supersaturation under these conditions. It was recommended, from the study, that controlling supersaturation and seeding can be implemented to control the rate of nucleation and enhance the rate of crystal growth in the antisolvent crystallization of REEs. Therefore, crystal engineering through supersaturation control offers several options through the knowledge of the antisolvent crystallization process to obtain the desired product.

Varying the antisolvent-to-solvent ratio maybe be a viable option to control supersaturation within the crystallizing system. Seeding can also be used in crystal engineering to control spontaneous homogeneous nucleation by promoting either secondary nucleation or crystal growth during crystallization. It has the potential to produce crystals that are easy to handle in downstream processes, such as filtration and drying (Loï Mi Lung-Somarriba et al., 2004). Seeding can induce crystallization at lower supersaturation, within the metastable zone by providing sufficient surface area for the supersaturation to be distributed (He et al., 2020; Mersmann, 2001).

1.2 Problem statement

The achievement of high yields in antisolvent crystallization often requires the use of large quantities of antisolvent. This is necessary to significantly reduce the solubility of the solute. Increasing the amount of antisolvent enhances the interaction between the antisolvent molecules and species in the aqueous phase (Kumar et al., 2014; Norouzi et al., 2020). This can potentially increase the degree of supersaturation in the crystallizer, resulting in excessive nucleation and the production of smaller or finer final particle sizes. These smaller particles are difficult to handle for downstream separation processes such as drying, washing, and filtration.

1.3 Project aim and objectives

This project aimed to investigate the effect of crystal engineering on product characteristics in batch antisolvent crystallization of neodymium sulfate. The objectives of this study were:

- To investigate the effect of varying the organic–to–aqueous (O/A) ratios on yield, particle size distribution (PSD), and morphology of the product in batch antisolvent crystallization of neodymium sulfate.
- To investigate the effect of seed loading on PSD and morphology of the product in batch antisolvent crystallization of neodymium sulfate.

1.4 Scope

The project presents an investigation into how crystal engineering influences final product characteristics in antisolvent crystallization. This was achieved using neodymium sulfate octahydrate which was chosen because of the high demand for neodymium. Eight-five percent of carmakers in 2021 were using neodymium-incorporated permanent magnet motors and, as of 2022, the projection for automotive demand for REEs was expected to rise by 25% (MordorIntelligence, 2022). The aqueous solution was limited to a synthetic leach solution mimicking the concentration of neodymium in the leach solutions from NiMH batteries as actual leach solution was not available. The project also involved thermodynamic modelling to predict theoretical yield and activity coefficients for neodymium and sulfate ions using OLI Stream Analyzer (11.0) (OLI-Systems-Inc, 2022).

1.5 Thesis outline

This thesis is presented in six chapters. The first chapter introduces the project, the problem statement, the aims, the objectives, and the scope of the project. Chapter 2 is a review of the theories of crystallization, with a particular focus on the fundamentals of antisolvent crystallization. Chapter 3 is a review of the existing literature on antisolvent crystallization and seeding. Chapter 4 presents the methodology used to investigate the problem. A discussion of results and key findings is done in Chapter 5. Chapter 6 provides the conclusions and recommendations for future work.

2 Theory

This chapter details the theory of antisolvent crystallization. Crystallization fundamentals such as supersaturation, nucleation, and growth, which are necessary to understand the antisolvent crystallization of REEs are presented.

2.1 Crystallization

Crystallization is a unit operation that involves a phase change of a compound from a fluid to a crystalline solid product (Lewis et al., 2015; Myerson et al., 2019). There are different types of crystallization which include antisolvent crystallization, melt crystallization, membrane, eutectic freeze crystallization, cooling crystallization, and evaporative crystallization. The selection of these processes is influenced by the final product characteristics desired (Lewis et al., 2015).

2.1.1 Antisolvent crystallization

Antisolvent crystallization occurs when a reduction in solubility is achieved by the addition of another solvent in which the solute is sparingly soluble to induce its crystallization or precipitation (Beckmann, 2013; Kaneko et al., 2002; Lewis et al., 2015). There are different terms used for antisolvent crystallization or precipitation which include salting out and drowning out.

The advantage of antisolvent crystallization is that it can be conducted at ambient temperatures, which is essential for heat-sensitive substances. This also makes the process convenient and economically viable (Myerson, 2002; Raj & Kurup, 2016). However, the downside of the process is that the binary solvent mixture must be separated later to recover and reuse one or both solvents. The added cost incurred during the separation process may be fully absorbed by the invaluable products recovered (Myerson et al., 2019).

At the point of antisolvent addition, there is bound to be high supersaturation that can result in excessive nucleation. Figure 2.1**.** shows different configurations for mixing the antisolvent and solvent for a compound that can form two polyforms. By adding the antisolvent to the solvent, the starting point for the mixing will be 100% solvent and 0% antisolvent. A relatively low supersaturation will be generated in the system as the solubilities are high. If the anti-solvent is added slowly, mild conditions will prevail and there will be a reduced chance of the formation of the undesirable metastable polymorph (Lewis et al., 2015).

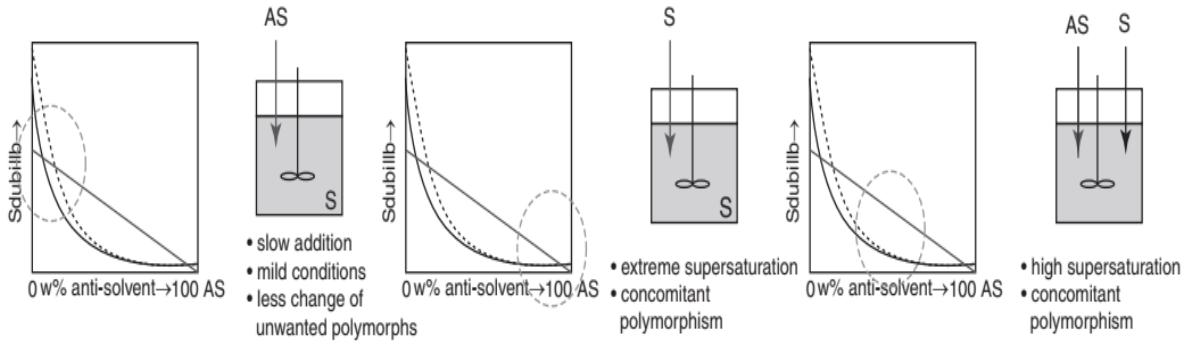

Figure 2.1: Effect of the addition configuration in anti-solvent crystallization (Lewis et al., 2015).

When the solvent is added to the antisolvent when solubilities are low, high supersaturation will be generated, leading to the formation of polymorphs. Polymorphism can be controlled by seeding in the metastable region or by seeding when the polymorphs start to form (He et al., 2020). When both the antisolvent and the solvent are added at the same time into the crystallizer, there is bound to be high supersaturation, leading to the formation of concomitant polymorphs (Lewis et al., 2015).

2.1.2 Supersaturation

Supersaturation is the driving force in antisolvent crystallization. Supersaturation control is extremely important to control the crystal size and crystal size distribution (CSD) (Mullin, 2001). Supersaturation in antisolvent crystallization is generated by physiochemical interactions between the antisolvent, solvent, and solute (Borissova et al., 2004). Primary nucleation is dominant at higher supersaturation, and this results in the production of smaller crystals. Faster crystal growth occurs at low supersaturation, resulting in the formation of larger crystal sizes.

Supersaturation ratio (S) can be calculated using equation 2.1;

$$S = \frac{\Pi\left(\gamma_i C_i\right)^{\upsilon_i}}{K_{sp}}, \qquad 2.1$$

where Υ_i and υ_i are the activity coefficient and units of species *i*, respectively. K_{SP} is the solubility product constant, which is calculated using equation 2.2:

$$K_{sp} = \Pi\left(\gamma_{i,\,eq} c_{i,\,eq}\right)^{\upsilon_i}, \qquad 2.2$$

where the subscript "*eq*" indicates equilibrium conditions.

Assumptions such as a low supersaturation or an activity coefficient ratio of one at supersaturated conditions do not apply to antisolvent crystallization (Myerson et al., 2019).

2.2 Nucleation

Nucleation can be primary or secondary. It is the formation of stable nuclei from a supersaturated solution (Mullin, 2001; Myerson et al., 2019). Primary nucleation occurs in a crystal-free environment while secondary nucleation occurs when there is a pre-existing crystal (Lewis et al., 2015).

2.2.1 Primary nucleation

Primary nucleation can be homogeneous or heterogeneous, depending on the action of foreign materials within the crystallizer. Homogeneous nucleation occurs spontaneously when there is no pre-existing foreign material. Heterogeneous nucleation occurs in the presence of foreign materials, such as surfaces or dust (Mullin, 2001).

The free energy change for a cluster formation resulting from homogeneous nucleation is calculated using equation 2.3 (Lewis et al., 2015; Mullin, 2001; Myerson et al., 2019; Randolph & Larson, 1988):

$$\begin{aligned}\Delta G &= \Delta G_{surface} + \Delta G_{volume} \\ &= 4\pi r^2 + \frac{4}{3}\pi r^3 \Delta G_{volume}, \end{aligned} \qquad 2.3$$

where $G_{surface}$ is the excess free energy between the surface of a particle and the bulk. It is a positive quantity. G_{volume} is the excess free energy between a very large particle and the solute in solution, which results when the solute changes from a liquid to a solid state. It is a negative quantity because the solid state is more stable than the liquid state. The radius of a cluster is represented by r.

Clusters that continuously decay and reassemble until they reach a critical size (r_c) are formed. At this critical size, the cluster becomes stable and grows into a crystal nucleus. Figure 2.2 shows the competition between the Gibbs surface free energy and the volume free energy.

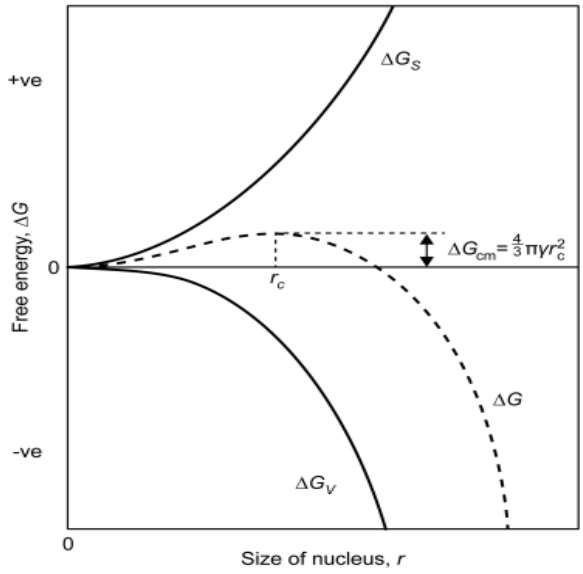

Figure 2.2: Gibbs free energy ΔG as a function of the radius of the cluster (Mullin, 2001).

The Gibbs free energy for the formation of stable nuclei as a function of supersaturation ratio (S) is given by equation 2.4 (Myerson et al., 2019):

$$\Delta G_{critical} = \frac{16\pi\sigma^3 v^2}{3(kT\ln S)^2}, \qquad 2.4$$

where: σ = interfacial free energy (Jm^{-2});

v = molecular volume (m^3mol^{-1});

k = Boltzmann constant (JK^{-1});

T = temperature (K);

S= supersaturation ratio (-).

2.2.1.1 Homogeneous nucleation

Homogeneous nucleation occurs at high supersaturations and the system must be free of foreign particles or surfaces, which is usually uncommon in practice (Mullin, 2001; Myerson et al., 2019; Ulrich & Jones, 2006). Homogeneous nucleation (*J*) is defined by equation 2.6, which shows that the nucleation rate decreases with an increase in surface tension and increases with an increase in supersaturation:

$$J = A\exp\left[-\frac{\Delta G_{critical}}{kT}\right]. \qquad 2.5$$

Substituting for $\Delta G_{critical}$ by equation 2.4 gives the expression for homogeneous nucleation:

$$J = A \exp\left[-\frac{16\pi\sigma^3 v^2}{3k^3T^3(\ln S)^2}\right], \quad 2.6$$

where *A* is the pre-exponential factor (nuclei/s).

2.2.1.2 Heterogeneous nucleation

Heterogeneous nucleation is initiated in the presence of foreign particles or impurities, such as dirt, dust, or surfaces, within the crystallizing system (Mullin, 2001). These foreign particles and surfaces reduce the activation energy barrier by reducing the surface energy of pre-nucleation clusters, which depends on the contact or wetting angle between the foreign particle or surface and the cluster (Myerson et al., 2019). Therefore, heterogeneous nucleation occurs at lower supersaturation than homogeneous nucleation (Myerson et al., 2019).

The rate of primary heterogeneous nucleation is calculated using equation 2.7:

$$J_{het} = A_{het}\exp\left[-\frac{16\pi\sigma^3 v^2 f(\phi)}{3k^3T^3(\ln S)^2}\right], \quad 2.7$$

where f(ϕ) is the correction factor for the reduced energy barrier. The relationship between the critical Gibbs free energy for homogeneous and heterogeneous primary nucleation is given by equation 2.8:

$$\Delta G^*_{het} = \phi \Delta G^*_{hom}, \quad 2.8$$

where ϕ is less than unity. The factor ϕ is related to the wetting angle, as expressed in equation 2.9 (Mullin, 2001):

$$\phi = \frac{(2+\cos\theta)(1-\cos\theta)^2}{4}, \quad 2.9$$

where θ is the contact or wetting angle. The contact angle indicates the measure or extent of the wettability of a solid by a liquid. It also indicates if the nucleation barrier will be lowered by the introduction of a foreign substance (Lewis et al., 2015). The relationship between the contact angle and the interfacial tension (σ) can be obtained using equation 2.10:

$$\cos\theta = \frac{\sigma_{sl} - \sigma_{cs}}{\sigma_{cl}}, \qquad 2.10$$

where: σ_{sl} is the interfacial tension between the liquid, l, and a foreign solid surface, s;
σ_{cs} is the interfacial tension between the solid crystalline phase, c, and foreign solid surface;
σ_{cl} is the interfacial tension between the liquid and the solid crystalline phase.

The contact angle ranges from 0 to 180^o, for a contact angle of 0^o, there is complete wetting, with the liquid spread over the foreign particle and no nucleation is necessary. The value of ϕ becomes zero and this happens when the substrate to be crystallized is identical to the foreign particle. This occurs when seeding is conducted in a supersaturated solution (Mullin, 2001). For a contact angle of 180^o, the liquid is not spread and foreign particles do not aid nucleation (Beckmann, 2013).

2.2.2 Secondary nucleation

Secondary nucleation occurs when there is already an existing crystal of the same solute to be crystallized from the supersaturated system and occurs at low supersaturations (Lewis et al., 2015; Mullin, 2001; Myerson et al., 2019). This can be categorised as contact, initial breeding, needle, and nucleation due to fluid shear breeding.

Initial or dust breeding usually occurs through the introduction of dry seed crystals to a solution. Crystals are formed from small fragments that are liberated from the surfaces of the seed crystals as these fragments act as new nuclei for crystallization (Myerson et al., 2019). Contact or attrition nucleation is the most common and important form of secondary nucleation. It results from collisions between the crystals and the impeller, between the crystals themselves, or between the crystals and the surfaces of the crystallizer (Lewis et al., 2015). The boundary layer between the solution and the crystal can also be a source of secondary nuclei due to turbulent fluid shear forces. A layer is removed from the adsorbed molecules into the solution, which then grows into crystals (Myerson et al., 2019).

At high supersaturations, needle or dendritic breeding occurs. Edges and corners of crystals are subjected to high supersaturation compared with the middle of the crystal-forming dendrites, and these protruding crystals break, resulting in secondary nuclei. Crystals also grow as bundles that can easily break (Lewis et al., 2015). Irregular polycrystalline aggregates

form very high supersaturations and they fragment, forming nucleation sites and leading to a phenomenon called polycrystalline breeding (Myerson et al., 2019).

2.3 Crystal growth

The growth stage, which immediately follows nucleation, is influenced by diffusion of growth units to the surface of already-formed nuclei and their integration into the crystal lattice structure (Khamskii, 1969). It includes a two-step process, i.e., mass transfer and a surface integration mechanism, as shown in Figure 2.3, where c_b is the bulk concentration, c_i is the concentration at the crystal and solution interface, and c_{eq} is the equilibrium concentration at the growth site. Growth involves the diffusion of growth units of the solute to the crystal surface, followed by the integration or arrangement of these growth units into the crystal lattice.

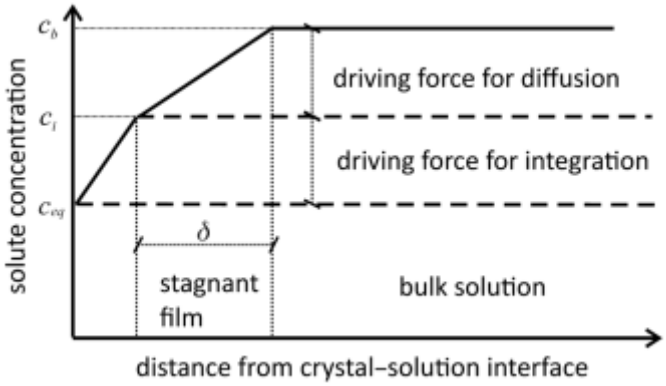

Figure 2.3: Concentration profile perpendicular to the crystal surface during growth (Nyvlt, 1984).

The rate of crystal growth is mainly affected by agitation rate, density, viscosity of the solvent, temperature, and trace impurities (Dhanaraj et al., 2010). Crystal growth happens on three sites of the crystal surface. At a terrace site, the growth units will attach only to the surface of the growing layer. At a step site, attachment of the molecule occurs at the surface and the growing step; for a kink site, the molecule attaches at all three surfaces (Myerson, 2002). At low supersaturations, a spiral growth mechanism is dominant and there are screw dislocations on kink sites, leading to smooth growth, as shown in Figure 2.4. Growth proceeds from layer upon layer. When supersaturation is increased, two-dimensional nucleation and growth become predominant due to the formation of 2 dimensional nuclei. Growth units

attach at any site on the crystal surface as the supersaturation is elevated, leading to rough growth of the crystal surface.

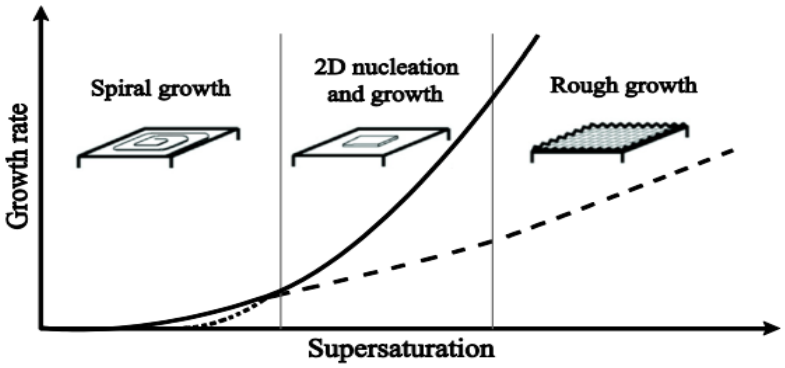

Figure 2.4: Progression of growth mechanisms (Lovette et al., 2008).

2.4 Agglomeration

Agglomeration is the process whereby particles stick or cluster together to form one bigger cluster. This can be termed aggregation, coagulation, or coalescence (Lewis et al., 2015). This phenomenon usually happens when there are small particles in the system and is hardly present for larger particles (Myerson et al., 2019). Unlike in crystal growth, where the number of particles remains the same, in agglomeration the number of particles is reduced (Mullin, 2001).

2.5 Seeding

Seeding is a process conducted to control spontaneous nucleation by promoting crystal growth conditions, mainly in batch crystallization processes (Mersmann, 2001; Palosaari et al., 2006). It is conducted in the metastable zone width, where supersaturation is low, to control the final product size, size distribution, and morphology to improve handling of the product in downstream processes, such as filtration, drying, and washing (Beckmann, 2013; Mullin, 2001). Supersaturation is consumed by crystal growth if the seeds provide sufficient crystal surface area to suppress secondary nucleation at lower supersaturation (Beckmann, 2013). Seeding has the advantage that it reduces the amount of antisolvent used, produces a consistent product, and greatly reduces the batch time of operation at an industrial scale (Korkmaz et al., 2020).

2.6 Morphology

Morphology refers to the external appearance or form of a crystal, and is also known as the crystal habit (Myerson et al., 2019). The final crystal morphology is often a result of the rate of growth, and is mainly determined by crystal faces that have the lowest growth rate because fast-growing faces grow out of existence (Mersmann, 2001; Myerson et al., 2019). Morphology is also influenced by parameters such as the type of crystallizer, properties of the crystalline solid, and mode of operation.

In antisolvent crystallization, changes in the solvent, supersaturation, or presence of impurities or additives affect crystal morphology to a high degree. Crystal morphology also affects downstream processes, such as filtration, drying, and milling, hence there is a need to control the crystallization process. Control of crystal morphology can be accomplished by choice of solvent, antisolvent, and additives into a solution; however, it is very difficult to achieve (Palosaari et al., 2006).

2.7 Additives and impurities

Impurities influence morphology, nucleation, and crystal growth. Soluble impurities can also affect the induction time of crystallization. Impurities are incorporated into the crystal surface and are deposited onto kink sites, steps, or terraces, thereby competing with regular growth units. The impact of surface-adsorbed impurities or additives is reduced when volume diffusion is the rate-controlling step. Rough growth, which occurs at higher supersaturation, is usually difficult to inhibit (Lewis et al., 2015).

2.8 Population balance equation

A population balance equation describes the evolution in time of the mass distribution of particles as a function of their sizes (Lewis et al., 2015). The population balance equation for characterizing the CSD in a batch crystallizer is calculated using equation 2.11 (Randolph & Larson, 1988):

$$\frac{\partial n}{\partial t} + G' \frac{\partial n}{\partial L} = 0 , \qquad 2.11$$

where n is the population density per unit suspension volume, G’ is the linear growth rate (ms^{-1}), L is the crystal size (m), and t is the batch time (s). Through the introduction of

moments, it becomes easy to solve the batch conversion equations because they are difficult to simultaneously solve. The moments of the CSD are defined as:

$$m_j = \int_0^{\infty} n(L)L^j dL \qquad \text{for } j = 0, 1, 2\ldots \tag{2.12}$$

where:

$$n(L)dL = \sum_i \frac{\text{Vol }\%_i \text{ x Conc (vol\%)}}{100} \text{ x } \frac{1}{k_v \bar{L}^3}, \tag{2.13}$$

Where: m_j is the respective moment;

vol% is the volume of the solids in a size range;

conc. (vol%) is the total concentration of solids (vol%);

n(L) is the number density function;

K_V is the volume shape factor.

The respective moments are calculated as (Lewis et al., 2015):

Total number $N_T = m_0$

Total length $L_T = m_1$

Total surface area $A_T = k_a m_2$, where k_a is the area shape factor

Total volume $V_T = k_v m_3$, where K_v is the volume shape factor

Total mass $M_T = \rho_{crystal} k_v m_3$

Examples of volume and surface shape factors for different crystal morphologies are presented in Table 2.1.

Table 2.1: Examples of shape factors (Mersmann, 2001).

Geometric shape	k_V	k_a
Sphere	0.524	3.142
Octahedron	0.471	3.464
Tetrahedron	0.118	1.732
Hexagonal prism	0.867	5.384
Cube	1.000	6.000
Needle 5 × 1 x 1	0.040	0.880
Plate 10 × 10 × 1	0.010	2.400

3 Literature Review

This section reviews previous work related to antisolvent crystallization, and the effects of varying O/A ratio and seeding on product quality. Section 3.4 summarises the hypothesis and research questions.

3.1 Antisolvent Crystallization

Antisolvent crystallization has mainly been used in the pharmaceutical industry more than in hydrometallurgy at an industrial scale (Peters et al., 2022; Vedantam & Ranade, 2013). However, it has been identified as an effective separation process in hydrometallurgy because it can produce high yields by the use of different organic solvents. Peters et al. (2019) reported the recovery of scandium as a salt from ammonium scandium hexafluoride using ethanol as an antisolvent. Kaya et al. (2018) investigated the recovery of scandium from an ammonium fluoride strip liquor using different organic antisolvents, such as methanol, isopropanol, ethanol, and acetone. The recovery of scandium from these studies was greater than 98% at an O/A ratio of 0.8.

Korkmaz et al. (2020) investigated the selective recovery of valuable metals from NiMH battery leach liquor by antisolvent crystallization using 2-propanol and ethanol as antisolvents. They observed that the total recovery exceeded 80%. Ma et al. (2020) reviewed the use of precipitation and crystallization in the production of metal salts for lithium-ion battery materials. The authors observed that if selective precipitation is conducted, further purification should be performed to obtain pure metal compounds. Nowee et al. (2008) noted that the yield and recovery of the final products are dependent on the purity of the antisolvent used. These studies prove that antisolvent crystallization can be used in hydrometallurgy to recover valuable metals; however, the selection of an antisolvent and the amount used are important and greatly influence the final product characteristics.

3.1.1 Effect of antisolvent addition method

An antisolvent can be introduced into a crystallizer through normal addition, where the antisolvent is added to the solvent, or by reverse addition, where the solvent is added to the antisolvent. At the point of antisolvent addition, there is bound to be high supersaturation that can result in excessive nucleation (Beckmann, 2013). The configuration of the antisolvent addition system is important in producing desired crystals.

Takiyama et al. (1998) found that poor mixing results in high local supersaturation at the point of addition and generates increased primary nucleation. Primary nucleation consequently leads to the formation of smaller or finer particles, which may agglomerate. O'Grady et al. (2007) confirmed that the addition of antisolvent close to the impeller improves homogeneous mixing and the incorporation of the antisolvent into the solution. The authors noted that the metastable zone width became wider when the antisolvent was added near the wall of the crystallizer. This was supported by Zhang et al. (2015) who noted that the increase in the metastable zone width was due to mixing efficiency differences between the two antisolvent addition locations.

Besides the addition point influencing the final product size, the rate at which the antisolvent is fed into the crystallizer also influences the crystallization process. Nowee et al. (2008) reported that higher antisolvent feed rates resulted in crystals of smaller sizes than those produced at lower feed rates. This was attributed to higher supersaturation levels generated at higher feed rates, resulting in higher nucleation rates. Yu et al. (2005) confirmed that, as the feeding rate increased the final product size was reduced. They deduced that at a higher feeding rate, the resulting particles exhibited a higher degree of agglomeration. The product obtained at a high feed rate had a smaller mean size compared with the lower feed rate, which had particles with sizes larger than 780 μm.

Waval et al. (2020) deduced that slow and simultaneous feeding of the antisolvent and the solvent to the crystallizer increased the average final crystal size. This observation agrees with those made by Peters et al. (2022), who reported that the final particle size increased at a lower feed rate. They noted that adding the antisolvent at a controlled low rate resulted in low generation of supersaturation, allowing crystal growth to be dominant. Ferguson et al. (2013) reported that a faster feed rate of antisolvent widens the metastable region, resulting in higher supersaturation at the point of addition, leading to a decrease in the mean particle size of the final product.

According to Lewis et al. (2015), adding an antisolvent to a solvent slowly can create low supersaturation and reduce the chances of forming undesirable polymorphs. Therefore, it is important to understand the effect of antisolvent addition location and feed rate on the final product crystals.

3.1.2 Effect of antisolvent-to-solvent ratio on particle size

Understanding the effects of the O/A ratio on solubility, supersaturation, nucleation, and crystal growth are essential in determining the resultant product obtained. Waval et al. (2020) noted that when the ratio of the antisolvent to solvent was increased from 0.1 to 0.4, the final average crystal size decreased from 320 to 220 µm. This was attributed to an increase in the nucleation rate due to higher levels of supersaturation. Hash and Okorafor (2008) agreed with these findings, in their study of batch antisolvent crystallization of sodium sulfate, they observed that as the quantity of methanol antisolvent increased, the mean crystal size decreased.

Peters et al. (2019) observed in the antisolvent crystallization of ammonium scandium hexafluoride, using ethanol as an antisolvent, that as the O/A ratio was increased, the product crystal size decreased due to increased supersaturation. Raj and Kurup (2016) also concluded that as the O/A ratio increased, the final particle size decreased significantly. An increased amount of antisolvent due led to an increased nucleation rate because of high supersaturation levels. These authors indicated that the critical size of the particle was inversely proportional to the logarithm of the supersaturation ratio.

However, from their study, Kumar et al. (2014) observed that although increasing the antisolvent-to-solvent ratio in the crystallization of cyclotrimethylenetrinitramine resulted in a decrease in particle size, at higher ratios (above 1:250) the particle size increased. Vorobei et al. (2016) concluded that an increase in the antisolvent-to-solvent ratio resulted in a decreased particle size until a certain threshold value, at which the particle size would start to increase. The decrease in particle size was attributed to high supersaturation levels. The increase in particle size after a certain threshold was attributed to smaller particles forming bridges between themselves because growth of the particles was assumed not to take place in isolation.

These observations are in agreement with the findings of Zhao et al. (2013), who observed that the mean particle size in the antisolvent precipitation of Genipin (A natural iridoid compound and the aglycone of geniposide isolated from the fruit of Gardenia jasminoides Ellis, used for the treatment of diseases in China) was reduced when the antisolvent-to-

solvent ratio was increased. The mean particle size then increased when the ratio was increased beyond a certain threshold value. This can be observed in Figure 3.1.

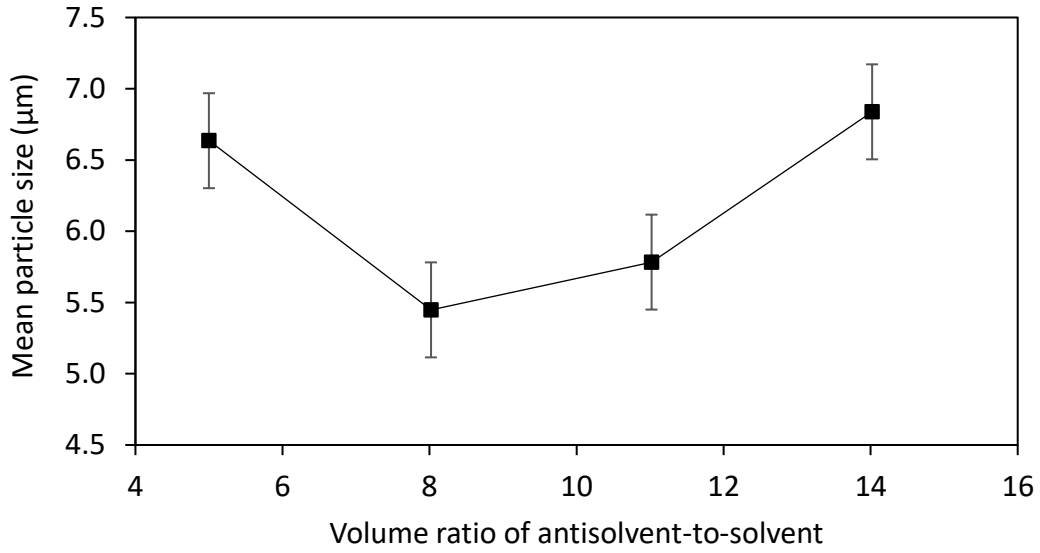

Figure 3.1: Effect of antisolvent-to-solvent volume ratio on the mean particle size of micronized Genipin (Zhao et al., 2013).

Norouzi et al. (2020) observed that the sphericity and particle size in the antisolvent crystallization of ammonium perchlorate initially decreased. This was due to increased interactions between the antisolvent and solvent molecules, resulting in higher supersaturation and production of smaller particles. However, they observed that as the O/A ratio was increased further to 1:4, the particle size increased. They deduced that the effect of the type of organic solvent used in the crystallization process was higher than the antisolvent-to-solvent ratio.

The findings indicate that varying the antisolvent-to-solvent ratio greatly influences the final product size. Therefore, it is important to know the behaviour or change in particle size as the amount of antisolvent is varied.

3.1.3 Effect of antisolvent and solvent on crystal morphology

Antisolvent crystallization has been found to influence the final crystal morphology or habit. Crystal morphology or habit is mainly influenced by external conditions or environment within the crystallizer and the internal structure of the crystal. It greatly influences downstream processes, such as drying, filtration, drying, and packaging (Yazdanpanah & Nagy, 2020).

Crystal morphologies can also be heavily influenced by changes in the roughness of the crystal surfaces. High supersaturations lead to rough growth or kinetic roughening on crystal surfaces, thereby influencing the resultant crystal morphology (Sleutel et al., 2008).

Peters et al. (2019) practically deduced that crystals of well-defined shapes and sizes finer than 2 µm were obtained during the antisolvent crystallization of ammonium scandium hexafluoride using ethanol. There was no significant change in crystal morphology as the O/A ratio was increased; however, the particle size was reduced.

Zhou et al. (2019) highlighted that the antisolvent influence is a result of interactions between the crystallizing solute and the antisolvent, which are mostly due to hydrogen bonds. In their study of antisolvent crystallization of 2,6-diamino-3,5-dinitropyrazine-1-oxide, the authors used dimethyl sulfoxide (DMSO) as the solvent and observed, that different crystal morphologies, such as needles, spherical clusters, and dendrites, were produced by varying different antisolvents, as shown in Figure 3.2.

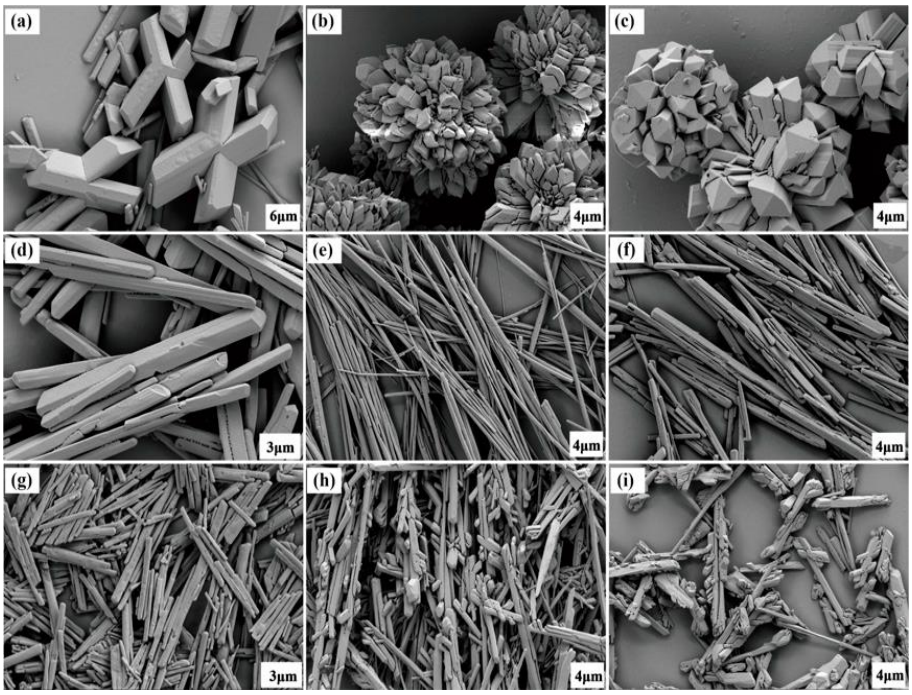

Figure 3.2: Scanning electron microscopy images of 2,6-diamino-3,5-dinitropyrazine-1-oxide crystals obtained by varying the antisolvent. (a) water, (b) methanol, (c) acetic acid, (d) nitromethane, (e) ethyl acetate, (f) ethanol, (g) methylene chloride, (h) o-dichlorobenzene, and (i) toluene (Zhou et al., 2019).

Zhou et al. (2019) observed that, intermolecular interactions between the antisolvent and solute molecules cause adsorption of the antisolvent onto different surfaces of the crystals affecting the nucleation, growth, and resultant morphology of the final crystals. However, the crystalline structure was not affected and did not change. It was observed that ethanol produced needle-like crystals because its polarity was medium compared with other antisolvents, such as methanol. Intermolecular interactions were influenced by the antisolvent polarity. The higher the polarity, the stronger the interactions. For example, the stronger polarity of methanol inhibited the growth of the crystal in the needle direction, resulting in spherical particles. Competition between the functional groups of the different antisolvents and the ion–dipole interactions of the solvent greatly influenced the supersaturation, thereby affecting the crystallization kinetics and final crystal morphology.

El Bazi et al. (2017) observed that an increase in the O/A ratio resulted in a reduced number of molecules of the solvent and therefore increased the resultant collisions between the solute molecules. Hence the nucleation kinetics were increased, and the growth rate was reduced in a water–alcohol mixture, causing a smoother crystal surface. Integration of solute growth units into the crystal lattice was also retarded by the adsorption of alcohol onto the crystal surface.

Xu et al. (2005) observed that ethanol molecules affected the morphology through interaction with hydrogen bonds on the crystal surfaces of ammonium dihydrogen phosphate and potassium dihydrogen phosphate. They concluded that the morphologies of these compounds changed from tetragonal prism and bipyramid to sharp needles as crystal development along the hydrogen bonds was inhibited by the suspension of a normal diffusion process.

Granberg et al. (1999) observed that the crystal morphology of paracetamol changed from rounded faces to rectangular due to an increase in acetone–water ratio. These findings indicate the influence of O/A ratio on the final crystal morphology. The literature highlights that using different antisolvents results in various crystal morphologies.

3.2 Seeding

Bergfors (2007) defined seeding as an optimization process conducted to control crystal growth conditions in crystallization. Seeding is a highly efficient method for stabilizing batch

crystallization and decreasing variations from batch to batch (Li et al., 2019; Parambil & Heng, 2017). Korkmaz et al. (2020) reported that seeding has the advantage of producing a consistent product in antisolvent crystallization of REE sulfates and that it has a direct impact on the time of operation at an industrial scale.

Seeding is normally done in the metastable zone width, where supersaturation is low, to control crystal size and CSD before spontaneous homogenous nucleation starts (Beckmann, 2013; Loï Mi Lung-Somarriba et al., 2004).

Kaya et al. (2018) and Peters et al. (2019) concluded that using a higher O/A ratio produces higher product yields. However, the final product sizes were minute (< 2 μm) and filtration and washing efficiencies were greatly reduced. Therefore, the authors recommended seeding to obtain a larger product size with a narrow PSD that is easier to handle and improve the effectiveness of downstream processes.

3.2.1 Factors affecting seeding.

Zhang et al. (2021) postulated that many factors affect seeding and, if not addressed, may lead to seeding failure in the crystallization process. The variables that need to be controlled to have a successful seeding include seed preparation, seed loading, seeding condition quality, and seeding mode.

3.2.1.1 Seed preparation, type, and quality

Seed quality entails the physical or chemical properties of the seeds used in the crystallization process. Rough surfaces on seeds can result in increased surface area for crystal growth. The quality and properties of the seeds are greatly influenced by the method of preparation used such as grinding, sieving milling, or washing (Kalbasenka et al., 2007).

Aamir et al. (2010) practically deduced the effect of seed preparation on seed quality, final product CSD, and morphology during batch cooling crystallization of potassium dichromate in water. They concluded that crystallized and sieved seeds produced final crystals with uniform and larger sizes. Milled, washed, and sieved seeds had fines from milling that led to initial breeding, production of crystals with no distinct shape, and agglomeration. Milling and sieving seeds resulted in the worst seed particles, with a lot of dust that led to initial breeding, Oswald ripening, large quantities of agglomeration, and less growth. Adi et al. (2007) concluded that wet sieving is an effective and preferable method used to produce particles with a narrow

distribution compared with milling, which produced very fine particles. However, both milling and sieving did not affect the crystallinity of the final lactose product.

Parambil and Heng (2017) demonstrated that milled seeds showed fractured edges and faces that had the potential to result in multiple crystal growth areas, resulting in agglomeration or other undesired growth effects. Seeds can also be washed and thereafter suspended in a slightly saturated solution before adding them to avoid initial breeding from dust particles and dissolution of the seeds (Aamir et al., 2010; Lakerveld et al., 2007; Lewis et al., 2015).

Seeds can be internally generated if seeding is to be conducted with the same material to be crystallized. This is called homogeneous seeding. Heterogeneous seeding is the use of a material that is different from the crystallized solute (Parambil & Heng, 2017). Warstat and Ulrich (2006) observed that using recrystallized seeds resulted in a process that is dominated by growth and that produced a narrow CSD.

Regy et al. (2002) investigated the recovery of struvite precipitation by seeding with sand and struvite, and concluded that sand seeding was not desired because the struvite did not coat the sand. These findings were supported by Ali and Schneider (2005), who also investigated the crystallization of struvite with different seed materials and realized that struvite seeds were more effective due to the similar structures and that the diffusion integration process was supported by the parent crystals. Borosilicate and silica had less–effective crystal growth and the final CSD showed smaller crystal sizes.

Wang et al. (2006) concluded in their findings that struvite powder produced the desired results when used as seeds to remove phosphorus in struvite precipitation compared with granite and sand. The solute coated onto the surface of the struvite powder and crystallized out, while for the granite and sand, there was no coating, and the product size was smaller. This was most probably because the contact angle was lower, and it reduced the nucleation barrier for heterogeneous nucleation, allowing the solute to spread onto the surface of the seed. However, when sand and granite were used, the contact angle was higher and therefore no wetting occurred. These findings agree with observations made by Ali and Schneider (2005) and Regy et al. (2002).

Jagadesh et al. (1996) investigated the effect of seed quality on the final product CSD using seeds of size 165 µm and 327.5 µm. The results of the products are shown in Figure 3.3. These authors concluded that the quality of seeds has no significant influence on the final product mean size, except for very large sizes of seeds that were ground.

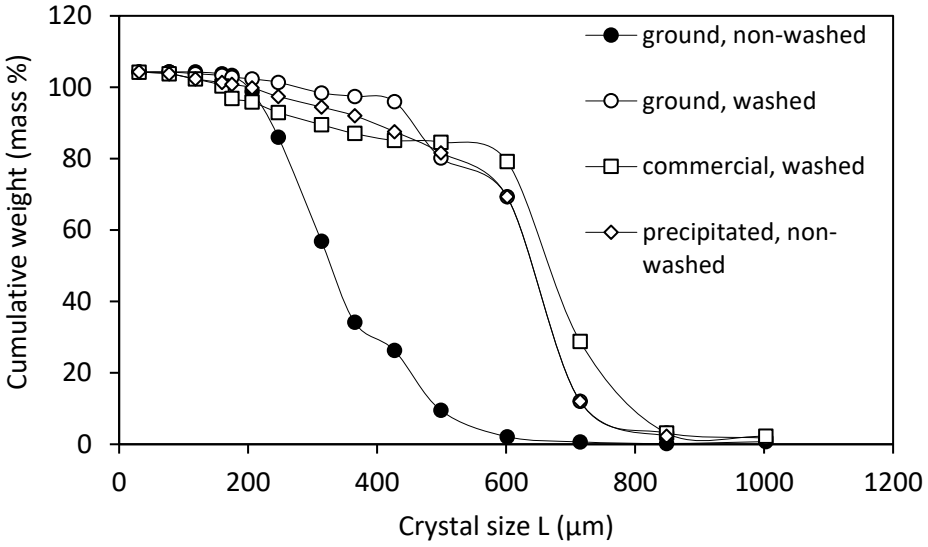

Figure 3.3: Effect of seed quality on crystal size distribution (Jagadesh et al., 1996).

These ground seeds resulted in improved performance of producing larger product mean size after the seeds were washed. Washing of the seeds removed dust particles, which possibly eliminated initial breeding. Initial breeding creates many nuclei within the system, thereby resulting in smaller final product crystals.

3.2.1.2 Seeding time

The timing of seed addition is very important in the crystallization process. If seeds are added too early, they can dissolve, and if added too late, heterogeneous primary nucleation will occur, resulting in excess nuclei and smaller product crystals. Therefore, seeds should be added at the beginning of batch crystallization (Lewis et al., 2015). According to He et al. (2020), the timing of seeding depends on the solubility properties of the solute to be crystallized, and seeding at lower supersaturation levels is effective to enhance secondary nucleation. Seeding should be conducted when the supersaturation is low because at higher supersaturation the dominant mechanism is nucleation, which results in smaller product crystals (Warstat & Ulrich, 2006).

3.2.1.3 Seed loading

Seed loading is a measure of the mass of seeds available per unit volume of the solution (Parambil & Heng, 2017). Important parameters to consider include seed mass, seed size, and seed size distribution. According to Parambil and Heng (2017), seed loading can be determined in terms of surface area and mass. At a lower seed mass, partial dissolution of the seeds may occur, resulting in the production of high levels of supersaturation (Lakerveld et al., 2007). In industrial processes, the seed mass used is between 2% and 6% of the theoretical mass to be crystallized out (Loï Mi Lung-Somarriba et al., 2004). The seed surface will provide an area for crystal growth, thereby minimising excessive primary nucleation within the system, and affecting the resultant crystal size and CSD. Loï Mi Lung-Somarriba et al. (2004) proposed an expression for the calculation of seed surface area, as shown in equation 3.1:

$$S_a = \frac{W_S\, k_a}{\rho k_v L_S} \qquad 3.1$$

where: S_a is the seed surface area (cm^2);

W_S is the seed mass (g);

L_S is the initial seed mean size (cm);

k_a is the surface shape factor (dimensionless);

k_v is the volume shape factor (dimensionless);

ρ is the crystal density (g/cm^3).

Smaller seed sizes provide a larger specific surface area, leading to a unimodal CSD (Kalbasenka et al., 2007). However, low seed loading is not desirable because it leads to a low surface area being available for crystal growth, which may lead to primary or secondary nucleation. The seed surface area available for crystal growth at a given seed loading ratio decreases with an increase in the available seed size (Jagadesh et al., 1996).

When the total surface area of seeds is insufficient for the supersaturation to be consumed, it leads to an increased number of smaller product crystals. These smaller product crystals are a result of excessive nucleation and the smaller particles may agglomerate (Palosaari et al., 2006). Therefore, enough seeds should be added to provide enough surface area to consume supersaturation and promote crystal growth (Beckmann, 2013).

The amount of seeds added to the crystallizer affects the final product crystals. Lewis et al. (2015) reported that very high seed loading is not desirable because a larger volume crystallizer is needed. Eder et al. (2011) observed that increasing seed loading resulted in the PSDs of product shifting to smaller particle sizes as shown in Figure 3.4. They concluded that an increase in seed loading resulted in an increased number of individual particles, which acted as crystallization sites where the solute was distributed, resulting in smaller sizes. Ward et al. (2011) substantiated this conclusion when they observed that an increased mass of seeds resulted in reduced growth as crystallization occurred on many nuclei within the crystallizer, which led to the solute being distributed on many seed crystals. This reduced the growth of individual seed crystals into larger product crystals.

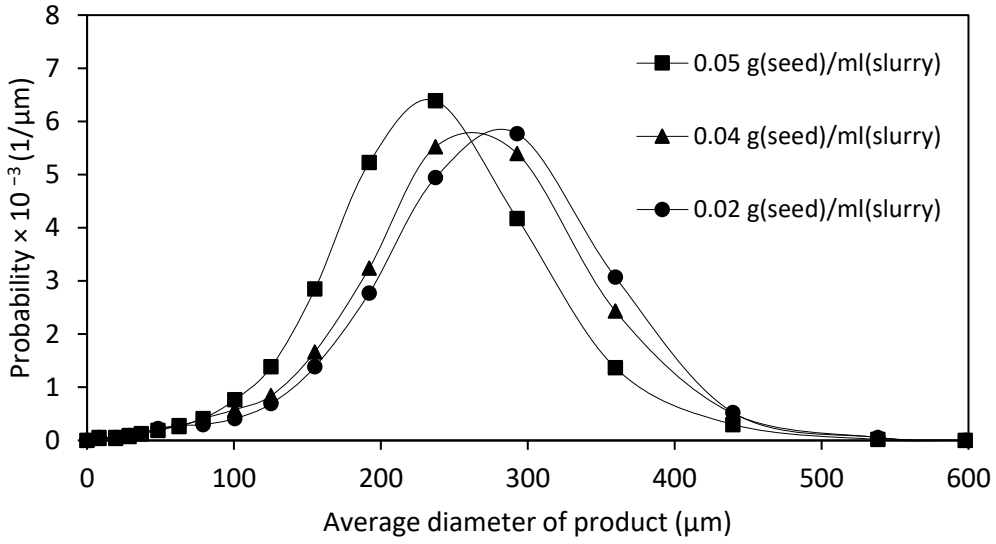

Figure 3.4: Product volume-density distributions of experiments with different seed loadings (Eder et al., 2011).

This was supported by Peters et al. (2022). In their study, the authors observed that increasing the seed loading beyond 20% of the theoretical yield (the amount expected to crystallize based on the starting point and final equilibrium value) resulted in smaller crystal sizes due to increased secondary nucleation. They attributed this decrease in size to the availability of a larger surface area on which the solute would be deposited. The optimal seed surface area observed was between a seed loading of 5% and 10%.

Seeding has the positive effect of producing a CSD or PSD that is unimodal. Yu et al. (2006) reported that increasing seed loading shortened the batch time and improved the PSD compared with low seed loading. They noted that when seed loading was doubled (corresponding to a seed loading ratio of 0.108), secondary nucleation was suppressed and the PSD was refined from multimodal to unimodal. Hojjati and Rohani (2005) observed that increasing seed loading decreased the supersaturation and promoted crystal growth, resulting in an improved CSD. At a low seed loading ratio (C_S) of up to 0.035, the final CSD was bimodal due to secondary nucleation. Warstat and Ulrich (2006) also observed that increasing the seed loading caused the CSD to become unimodal.

Kubota et al. (2001) concluded that at a high seed loading ratio (C_S = 0.33) above a critical point, unimodal grown seeds were obtained in a batch cooling crystallization of potassium alum. At a low seed loading ratio (C_S = 0.051), the CSDs obtained were bimodal. Loï Mi Lung-Somarriba et al. (2004) corroborated this conclusion when they observed that there is a critical seed mass beyond which a unimodal CSD can be obtained. Using a seed mass below the critical mass resulted in a bimodal final CSD. Doki et al. (2022) agreed with these findings, in their study of batch-cooling crystallization of sucrose. The authors observed that at high seed loading ratios (C_S = 0.15) and seed size of 328 µm, the CSD became unimodal.

Doki et al. (1999), developed a correlation to determine the critical seed loading C_S*, shown in equation *3.2*. They defined C_S* as the lowest value of seed loading that is required to suppress nucleation:

$$C_S^* = 2.17 \text{ X } 10^{-6} L_{seed}^2 , \qquad 3.2$$

where: L_{seed} is the seed size (µm).

Doki et al. (2001) confirmed that seed loading below the critical seed loading resulted in bimodal CSDs as the number of particles was too low to suppress nucleation however; at high seed loading, the CSDs were unimodal. Kubota et al. (2001) also concluded that at seed loadings above the critical point, unimodal CSDs were obtained.

Wang and Ward (2015) observed that it was not possible to entirely suppress the nucleation of barium sulfate by seeding. A critical seed loading ratio of 0.0162 using a small seed size (5

μm) and larger mass (0.290 kg/m^3) was insufficient to suppress nucleation. The authors observed a bimodal CSD, with peaks at smaller crystal sizes showing nucleated crystals. However, they deduced that at larger seed sizes (50 μm) and lower mass (9.9 g/m^3), which gave a seed loading ratio of 0.011, nucleation was greatly suppressed at the calculated critical seed loading. Warstat and Ulrich (2006) reported that the use of smaller seed sizes resulted in a decreased total number of product crystals. This indicated that agglomeration might have occurred during crystallization.

Larger seed sizes are often not advisable to use as they result in attrition and uncontrolled nucleation (Loï Mi Lung-Somarriba et al., 2004). Yu et al. (2006) observed that larger seed crystal sizes of 212–250 μm caused secondary nucleation due to attrition which gave rise to new nuclei within the crystallizer. They concluded that using finer seed particles of size 150 – 180 μm can greatly reduce secondary nucleation. However, Loï Mi Lung-Somarriba et al. (2004) found that using smaller seeds of size between 250 μm and 1600 μm resulted in faster production of large crystals of well-defined morphology for batch–cooling crystallization of glycine. Beckmann (2013) postulated that smaller seed particles tend to agglomerate, leading to reduced surface area available for crystal growth. The resultant effect is an agglomeration of product crystals.

Gao et al. (2018) reported that using a uniform seed size distribution resulted in a narrow final CSD. A wider seed size distribution leads to a wider CSD, which is undesired. This observation agrees with the conclusion by Yu et al. (2006) that undersized seeds obtained from an existing production unit produced a unimodal PSD of the product because the undersized seeds were not in a narrow range.

3.3 Critical synthesis/gap analysis

Numerous studies have been conducted to understand batch antisolvent crystallization and the characteristics of the product crystal (Hash & Okorafor, 2008; Kumar et al., 2014; Waval et al., 2020). However, the literature reviewed showed that most work on antisolvent crystallization has been carried out in the pharmaceutical industry and not in hydrometallurgy. Therefore, this work aimed at understanding the antisolvent crystallization of REEs, exemplified by neodymium sulfate.

The main challenge in batch antisolvent crystallization is to produce a consistent product of uniform CSD and size (Aamir et al., 2010). It is, therefore, important to control the rate of supersaturation in antisolvent crystallization (Peters et al., 2019). Crystal engineering provides a pathway for achieving this by seeding and controlling the O/A ratio.

It has been presented in the literature that the antisolvent feed rate and location of addition into the crystallizer greatly influence the final product crystal characteristics. Higher feed rates result in smaller final product crystals (Nowee et al., 2008; Yu et al., 2005), while slow addition of the reagents results in the formation of particles with a larger final size (Lewis et al., 2015; Waval et al., 2020). It was also highlighted that the antisolvent should be added closer to the impeller to improve the mixing efficiency within the system (O'Grady et al., 2007; Zhang et al., 2015).

An analysis of previous studies has shown that varying the antisolvent-to-solvent ratio results in two possible scenarios: the product crystal size increases with an increase in the O/A ratio (Hash & Okorafor, 2008; Raj & Kurup, 2016; Waval et al., 2020); however Kumar et al. (2014); Vorobei et al. (2016), and Zhao et al. (2020) found that the product crystal size became smaller as the antisolvent-to-solvent ratio was increased.

The literature also shows that different crystal morphologies are obtained due to interaction of the antisolvent and solvent. The morphologies vary from needles to prisms, platelets, spherical clusters, and squares as a result of the change in the antisolvent–to–solvent ratio (Charmolue & Rousseau, 1991; Garg & Sarkar, 2016; Holmbäck & Rasmuson, 1999; Xu et al., 2005; Zhou et al., 2019). It is important to investigate how varying the antisolvent-to-solvent ratio would affect the size and CSD of product crystals in batch antisolvent crystallization of neodymium sulfate. The influence of this approach on the morphology of the product crystals is currently limited.

The effectiveness of seeding in controlling crystal size and CSD has been reported mainly in batch–cooling crystallization of organic compounds (Aamir et al., 2010; Kubota et al., 2001; Warstat & Ulrich, 2006). Different seed sizes and seed loadings have been used in the reviewed literature; however, there is no agreement on a particular seed size to use or seed loading. It has been noted that there is a critical seed loading above which the desired results of a unimodal CSD and final crystal size are obtained (Doki et al., 1999; Kubota et al., 2001;

Loï Mi Lung-Somarriba et al., 2004). Therefore, critical seed loading provides a basis on which seeding can be conducted to inhibit nucleation and promote crystal growth (Doki et al., 1999).

It is, therefore, imperative that an investigation into how crystal engineering can be used to control supersaturation and achieve desired product crystals that are easier to handle for downstream processes be conducted. This is because at a higher O/A ratio the product yield is high; however, there is a downside of producing fine crystals.

3.4 Hypothesis and key questions

3.4.1 Hypothesis 1

Increasing the O/A ratio will result in smaller product particle sizes of neodymium sulfate. This is because as the O/A ratio is increased, the degree of supersaturation within the crystallizer increases which leads to high nucleation rates resulting in smaller particles.

i. How does varying the antisolvent-to-solvent ratio influence the characteristics of the product particles in the antisolvent crystallization of neodymium sulfate?
ii. How does batch time affect product characteristics at different O/A ratios?

3.4.2 Hypothesis 2

Introducing seeds will help in providing a surface area for crystal growth, thereby controlling primary nucleation, and producing larger product particle sizes with a narrow PSD.

Increasing seed loading decreases the mean product particle size and results in a wider PSD. This is because, with an increase in the number of seed particles, the solute is distributed on a higher number of seed particles, hence limiting linear growth rate of crystals. An increase in the total number of particles within the system leads to a higher number of collisions, resulting in breakages and the formation of many nuclei, leading to the formation of a wider PSD.

i. What is the effect of seed loading on particle size, PSD, and morphology in the antisolvent crystallization of neodymium sulfate?
ii. What is the effect of seed loading on the filterability of the neodymium sulfate product?

4 Materials and Methods

Section 4.1 details the thermodynamic modelling conducted. This is followed by section 4.2 that describes the experimental design. Preparation of the solution and seeds used in the experiments are described as is the analytical equipment used. The experimental procedure used is explained and the method used to harvest the product is outlined.

4.1 Thermodynamic modelling

Thermodynamic modelling, to predict the theoretical yield of neodymium sulfate octahydrate [$Nd_2(SO_4)_3.8H_2O$] and activity coefficients for neodymium and sulfate ions, was conducted using OLI Stream Analyzer 11.0 (OLI-Systems-Inc, 2022). The software calculates or predicts speciation, chemical and phase equilibria in multi–component systems. The Mixed Solvent Electrolyte (H_3O^+ ion) thermodynamic framework was used because it has better predictions for multi–component systems with competing solid phases (OLI-Systems-Inc, 2022).

It was assumed that the NiMH battery leach solution was an ideal solution which was very dilute. It was further assumed that the leach solution contained a single component, neodymium sulfate at a concentration of 3.5 g/L. A temperature of 25°C, pressure of 1 atm and 1 L of leach solution were assumed.

The activity coefficient model covers a wide range of chemistries (electrolyte, non-electrolyte, and mixed systems). To calculate activity coefficients in the mixed solvent electrolyte the excess Gibbs energy is constructed as a sum of three terms:

$$\frac{G^{ex}}{RT} = \frac{G^{ex}_{LR}}{RT} + \frac{G^{ex}_{MR}}{RT} + \frac{G^{ex}_{SR}}{RT} \quad , \tag{4.1}$$

Where G_{LR}^{ex}, G_{MR}^{ex}, G_{LR}^{ex} represent the long, middle, and short-range contributions respectively. The long–range term is calculated from Pitzer–Debye–Hückel formula and the short–range term from UNIQUAC equation. The middle term, which is key to representing electrolyte properties, is calculated from an ionic strength–dependent, symmetrical second virial coefficient–type expression (OLI-Systems-Inc, 2022). The activity coefficient (Υ) will be given by the following expression:

$$\ln \gamma_i = ln(\gamma_i^{LR}) + ln(\gamma_i^{MR}) + ln\left(\gamma_i^{SR}\right) \quad , \tag{4.2}$$

4.2 Experimental Design

Table 4.1 summarises the experimental plan. The first set of experiments was conducted to investigate the effect of varying the organic to aqueous (O/A) ratios on product yield, PSD, and morphology of $Nd_2(SO_4)_3.8H_2O$ product. The second set of experiments was conducted to determine the evolution of moments of PSDs at different batch times. The third set of experiments was conducted to investigate the effect of seed loading on the PSD and morphology of the $Nd_2(SO_4)_3.8H_2O$ product.

Table 4.1: Summary of Experimental plan.

Aim		Controlled Variables	Measured Variables
1	To investigate the effect of varying O/A ratios on $Nd_2(SO_4)_3.8H_2O$ product yield, PSD, and morphology in batch antisolvent crystallization.	O/A ratio (0.6; 0.8; 1.0; 1.2; 1.4.).	• Yield • PSD • Crystal morphology.
2	To determine the phenomena causing size enlargement between O/A ratios of 0.8 and 1.4. Evolution of moments was conducted.	• O/A ratio (0.8 and 1.4) • Batch time (0.25 h, 0.5 h, 1.0 h, and 2.5 h)	• PSD • Crystal morphology
3	To investigate the effect of seed loading on the PSD and morphology of $Nd_2(SO_4)_3.8H_2O$ product in batch antisolvent crystallization.	Seed loading (0.64%, 5%, 10%, and 20%).	• PSD • Crystal Morphology • Filtration time

4.3 Synthetic solution preparation

$Nd_2(SO_4)_3.8H_2O$, with 99.9% purity (ThermoFisher (Kandel) GmbH, Germany), was weighed on a digital scale (Radwag AS220.R2 Plus, Radwag Electronics, Radom, Poland) and dissolved in deionised water to make a 3.5 g/L $Nd_2(SO_4)_3$ synthetic leach solution. The synthetic leach solution mimicked the concentration of $Nd_2(SO_4)_3$ in leach solutions from NiMH batteries (Korkmaz et al., 2020). The aqueous solution was filtered through a 0.22 µm nylon membrane filter supported by a Merck Millipore glass holder. A Vacutec oil-less piston vacuum pump connected to a filter flask was used for filtration. The residue was left to dry for five days at room temperature (22 ± 2°C). After five days, the mass was constant, and it was assumed that drying had been completed.

4.4 Seed preparation

$Nd_2(SO)_4.8H_2O$ product was recovered from experiments conducted at an O/A ratio of 0.4 and was used as seeding material. The product obtained at O/A = 0.4 was granular and had well-defined morphology, hence it was used as seeds. The PSD of the $Nd_2(SO_4)_3.8H_2O$ seeds used in the experiments is shown in Figure 4.1. The seeds were chosen to take into consideration the studies by Regy et al. (2002) and Ali and Schneider (2005), who concluded that seeding with the same material to be crystallized produced desired results.

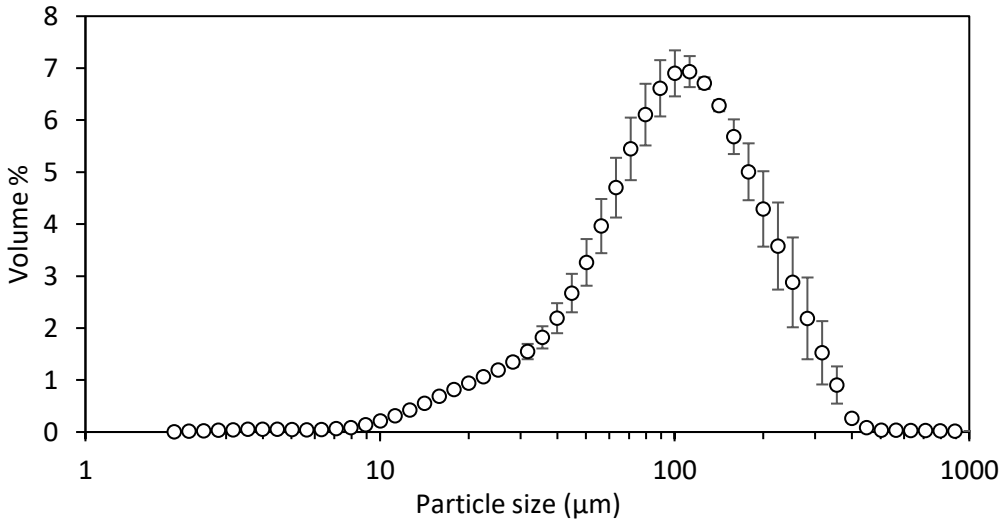

Figure 4.1: Particle size distribution of $Nd_2(SO_4)_3 .8H_2O$ seeds.

The mean particle size of the seeds was 117.2 µm. The seed surface area was calculated using equation 3.1 showing that the surface area increased from 18.7cm^2 to 598 cm^2 when the seed loading was increased from 0.64% to 20%, as presented in Appendix A1. The morphology of the seeds used is shown in Figure 4.2.

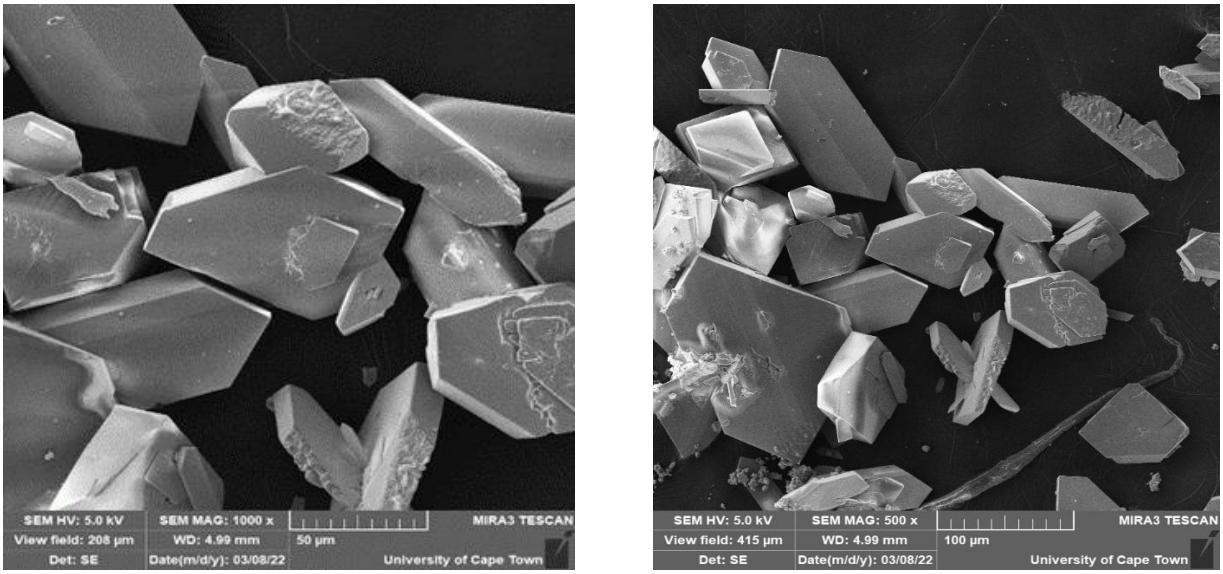

(a) (b)

Figure 4.2: Scanning electron microscope micrograph of seeds used (a) scale bar 50µm, (b) scale bar 100 µm.

4.5 Experimental Equipment

All experiments were conducted with a 500 mL baffled glass batch crystallizer, as shown in Figure 4.3. The crystallizer had three baffles, and a diameter of 0.08 m. Two Watson Marlow 520S peristaltic pumps (Watson-Marlow Bredel S.A. (Pty) Ltd., Johannesburg, South Africa) were used to pump the aqueous leach solution and the antisolvent, which was ethanol (99.9 % from KIMIX Chemical and Lab Supplies). A digital overhead stirrer (IKARW 20, IKA, Staufen, Germany), which was connected to a stainless steel six-blade Rushton turbine impeller, was used to provide mixing at a Reynolds number of 11 000. The impeller diameter was 0.03 and it was placed centrally at a clearance from the bottom of the crystallizer that was equal to one third of the total height of the crystallizer. Glass conical flasks were used for the storage of ethanol and the aqueous solutions.

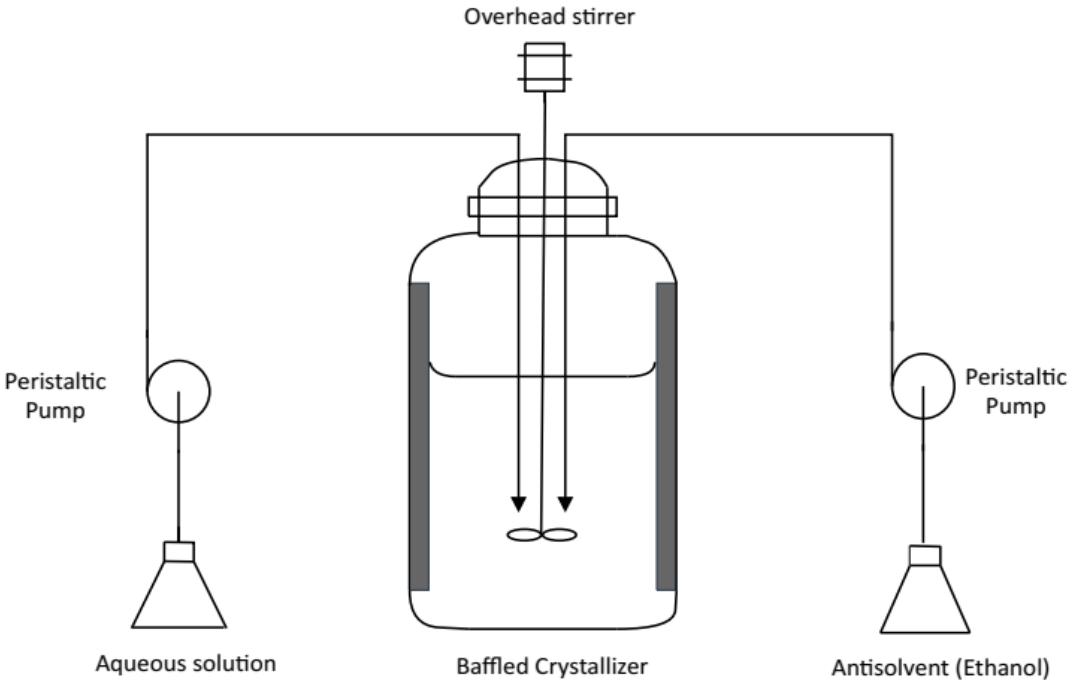

Figure 4.3: Baffled batch crystallizer with an overhead stirrer held on a stand.

4.6 Analytical Equipment

A laser diffraction particle size analyzer (Malvern Mastersizer 2000, Malvern Panalytical, Malvern, UK) was used to measure the PSD and particle size. Crystal morphology was determined using images that were obtained from a Tescan MIRA3 Rise Scanning Electron Microscope (SEM, Wirsam Scientific, Johannesburg, South Africa). Images were obtained at different magnifications of 10 000; 5000[; 1000; and 500. At least 30 images were acquired at each set of conditions including, repeats (e.g., at an O/A ratio of 0.8) to improve representativeness of the analysed sample.

4.7 Experimental Procedure

Experiments were conducted in three phases. All experiments were conducted in triplicate and randomised. For each set of experiments the filtrate from the $Nd_2(SO_4)_3$ aqueous solution was used as the synthetic leach solution. The aqueous synthetic leach solution and ethanol (antisolvent) were stored in separate conical flasks. These were then simultaneously pumped into the crystallizer close to the impeller to ensure constant O/A ratios and mixing at any given time. The stirrer was started before ethanol and the aqueous solution were fed into the crystallizer and the fluid motion was turbulent at a Reynold's number of 11 000. Table 4.2 shows the flowrates used in the experiments.

Table 4.2: Flowrates of reagents at different organic–to–ratios.

O/A ratio	Ethanol flowrate (mL/min)	$Nd_2(SO_4)_3$ aqueous Leach Solution flowrate (mL/min)
0.6	60	100
0.8	80	
1.0	100	
1.2	120	
1.4	140	

4.7.1 Varying organic–to–aqueous ratio

For the first set of experiments, O/A ratios of between 0.6 and 1.4 (0.6, 0.8, 1.0, 1.2, and 1.4) were used. Experiments to determine the effect of varying the O/A ratios on product characteristics were run for a batch time of 2.5 h at each O/A ratio.

4.7.2 Evolution of moments

For the second set of experiments, different batch times were used to calculate the evolution of moments. The batch times used were 0.25 h, 0.5 h, 1.0 h, and 2.5 h.

4.7.3 Effect of seed loading on product characteristics

The effect of seed loading on the PSD and crystal morphology of the precipitate was investigated at an O/A ratio of 1.4. This O/A ratio was selected because maximum yield of the product was obtained at this O/A ratio but filtration of the precipitate was poor.

The critical seed loading was quantified using equation 3.2 and was found to be 2.98% of the theoretical yield. Seeding was then conducted at seed loadings between 0.64% and 20% of the theoretical yield by mass (0.64, 5, 10, and 20%). This range of seed loading covered values below and above the estimated critical seed loading.

$Nd_2(SO_4)_3.8H_2O$ seeds were added to the crystallizer before the aqueous solution and ethanol were added. This was to ensure that the seeds were available in the reactor before the initiation of crystallization. The stirrer rotational speed was enough to suspend the seeds and products at O/A ratios, The batch time for seeding experiments was set at 2.5 h.

4.8 Harvesting

After each experimental run, a sample of the product slurry was collected for PSD measurement using laser diffraction. The vacuum pump, connected to the filter flask, was

started, and the remaining slurry from the crystallizer was poured into the filter funnel, connected to the filter flask, for filtration. At the same time, a stopwatch was started to measure the duration of filtration. At the end of the filtration, the duration was recorded and the product was harvested for drying. The recovered product was dried for five days at room temperature (22 ± 2°C). After five days, the final mass was constant, and it was assumed that drying had been completed to determine the yield. Equation 4.3 was used for calculating yield.

$$\text{Yield } (\%) = \frac{\text{mass of the dry precipitate}}{\text{mass of dissolved } Nd_2(SO_4)_3.8H_2O} \times 100 \qquad 4.3$$

A sample of dried precipitate was collected for image analysis.

5 Results and Discussion

This chapter presents the results obtained from the investigations conducted and the interpretation of the results. Section 5.1 focuses on the effect of varying the O/A ratios on the product characteristics. Section 5.2 focuses on the effect of seed loading on the final product characteristics. The product characteristics considered in these investigations include yield, particle size, PSD, and morphology.

5.1 Effect of varying organic–to–aqueous ratios on the yield of $Nd_2(SO_4)_3.8H_20$ product

The effect of varying the O/A ratios by increasing the amount of ethanol on the yield of $Nd_2(SO_4)_3.8H_2O$ product recovered from the synthetic leach solution is shown in Figure 5.1. The theoretical yield (the amount expected to crystallize based on the starting point and final equilibrium/solubility value) of the solute when ethanol was added to the aqueous solution was predicted from thermodynamic modelling using OLI Stream Analyzer (11.0). There was a significant increase in the theoretical yield as the O/A ratio was increased from 0.6 to 1.4.

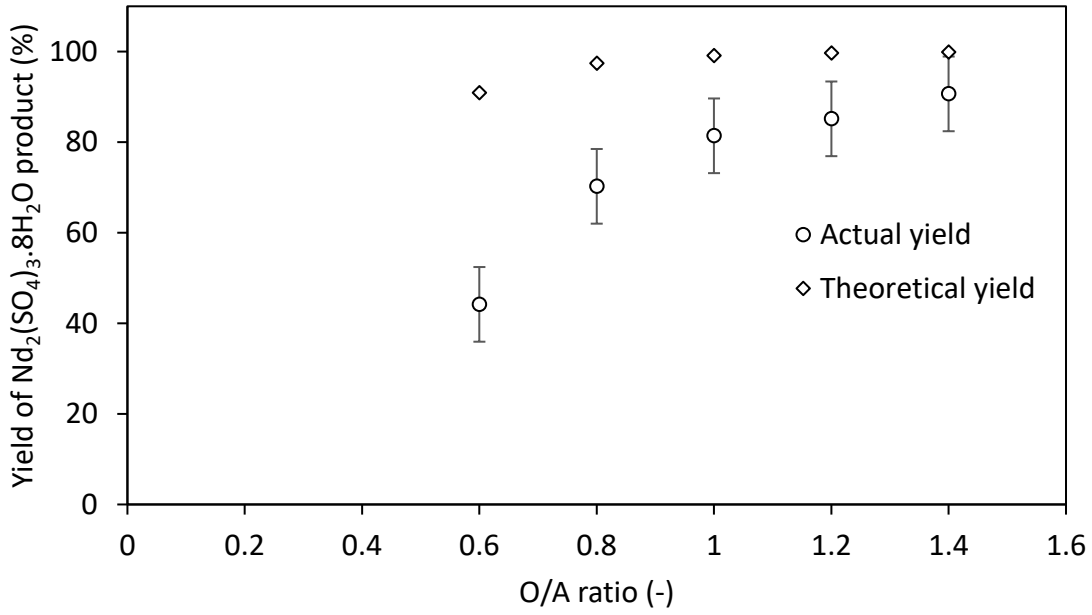

Figure 5.1: Yield of $Nd_2(SO_4)_3.8H_2O$ product at different organic–to–aqueous ratios.

Increasing the amount of ethanol from an O/A ratio of 0.6 to 1.4 increased the actual yield of $Nd_2(SO_4)_3.8H_2O$ product. This was due to the reduction in the solubility of neodymium sulfate as the amount of ethanol was increased, which caused its crystallization. These results are in

agreement with the work carried out by Peters et al. (2019) and Korkmaz et al. (2020), who concluded that increasing the amount of antisolvent results in an increased product yield. In their studies, they observed that the optimal O/A ratio for maximum yield was 0.8. This is supported by the theoretical yield curve in Figure 5.1 which shows the curve approaching a constant value between 0/A of 0.8 and 1.4. However, the actual yield shows that increasing the O/A beyond 0.8 results in a further increase in the product yield, and the curve shows that it may approach a maximum value beyond an O/A ratio of 1.4.

The significant difference between the theoretical yield and actual yield can be attributed to difference in the final solubilities between the model and the actual experiment. The solubility for the model in predicting the theoretical yield was very low compared with the experimental solubility. The difference can also be attributed to the batch time of 2.5 h used in the experiments compared with that used by Korkmaz et al. (2020) of between seven and ten days. A single experiment was conducted for a longer batch time of more than 24 h at an O/A ratio of 0.6. It was noted that the actual yield increased to more than 80%, as more solute crystallized out. This shows that at higher O/A ratios the yield will possibly approximate a maximum.

5.2 Effect of varying organic–to–aqueous ratio on the characteristics of $Nd_2(SO_4)_3.8H_2O$ product

5.2.1 Effect of varying organic–to–aqueous ratio on the particle size distribution and particle size of $Nd_2(SO_4)_3.8H_2O$ product

The effect of varying the O/A ratio by increasing the amount of ethanol on the particle size and PSD of the $Nd_2(SO_4)_3.8H_2O$ product recovered from the synthetic leach solution was investigated. The results obtained at O/A ratios of 0.8, 1.0, 1.2, and 1.4 are shown in Figure 5.2. The PSD at the O/A ratio of 0.6 could not be measured as the yield was insufficient for analysis with laser diffraction.

The peaks of the PSDs in Figure 5.2 shifted to lower particle size as the O/A ratio increased from 0.8 to 1.4. This showed that increasing the amount of ethanol (i.e., O/A ratio from 0.8 to 1.4) increased the particle sizes.

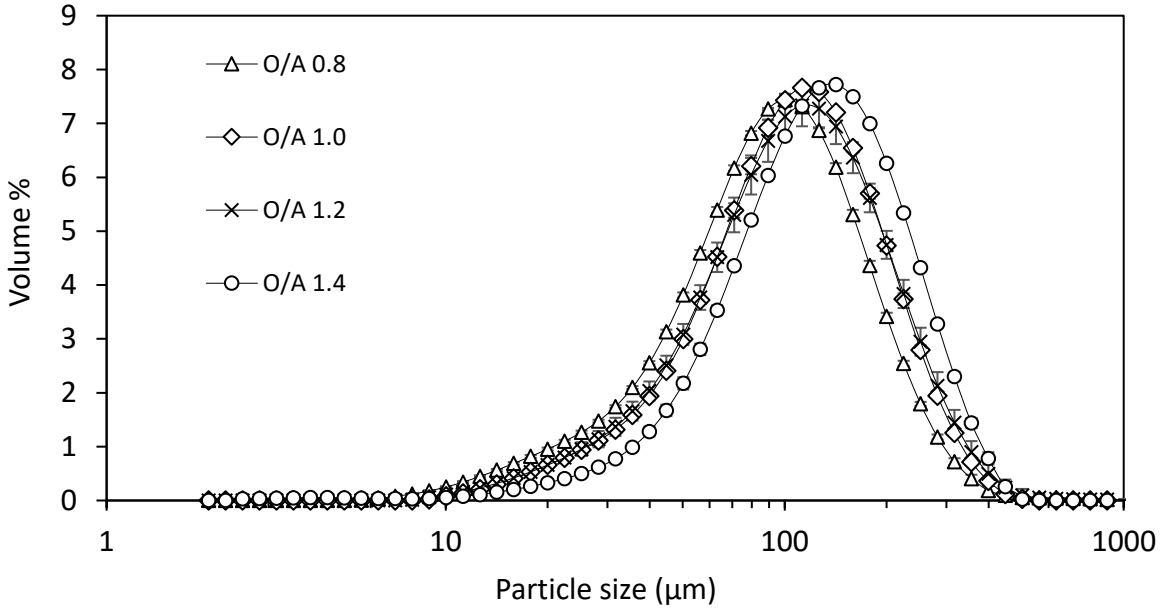

Figure 5.2: Effect of varying organic–to–ratio on the particle size dostribution of $Nd_2(SO_4)_3.8\ H_2O$.

A summary of the particle sizes obtained is presented in Table 5.1. The mean, mode, D_{10}, D_{50}, and D_{90} all increased as the O/A ratio increased. These results substantiate the PSDs results that the particle sizes increased as the O/A ratio increased. However, there was an insignificant increase in the particle sizes when the O/A ratio was increased from 1.0 to 1.2. It is not clear what caused this behaviour; however, it can be attributed to the supersaturations at these O/A ratios being in the same range.

Table 5.1: Summary of particle sizes of $Nd_2(SO_4)_3.8\ H_2O$ product obtained at different organic–to–ratios.

O/A ratio	Mean (µm)	Mode (µm)	D_{10} (µm)	D_{50} (µm)	D_{90} (µm)
0.8	106.1	100.2	31.5	86.7	181.7
1.0	120.8	112.5	39.9	100.8	205.4
1.2	123.7	112.5	39.1	101.1	213.6
1.4	141.4	141.6	49.9	119.2	238.4

The increase in particle sizes as the O/A ratio increased was unexpected because higher O/A ratios are expected to increase the degree of supersaturation, which would cause excessive nucleation and produce smaller particles (Peters et al., 2019; Raj & Kurup, 2016; Waval et al.,

2020). When the O/A ratio was increased from 0.8 to 1.4, the degree of supersaturation, calculated using equation 2.1, increased from 5.20×10^5 to 4.23×10^{11} (see Appendix A2). The increase in supersaturation was expected to enhance the rate of nucleation of $Nd_2(SO_4)_3.8H_2O$ but it appeared as if these conditions promoted the size-enlargement of the particles.

However, a possible explanation can be that the smaller particles agglomerated to form bigger particles, as highlighted by Vorobei et al. (2016). It was unclear which size-enlargement mechanism occurred at the higher supersaturations. Therefore, it was important to determine the mechanism that caused the increase in particle size as the O/A increased. The evolution of moments is explored in Section 5.2.3 to identify the mechanisms that influenced the sizes of particles at high O/A ratios.

5.2.2 Effect of varying organic–to–aqueous ratio on $Nd_2(SO_4)_3.8H_2O$ product crystal morphology

SEM micrographs of the $Nd_2(SO_4)_3.8H_2O$ products obtained at different O/A ratios are presented in Figure 5.3 and Figure 5.4. The micrographs represent the same sample taken at different magnifications of 1000 x and 500 x respectively. The micrographs show that the precipitate consisted of tabular, plate-like crystals, which became thinner, smaller, and asymmetric as the O/A ratio increased from 0.8 to 1.4. For the O/A ratios of 0.6 and 0.8, the crystals were well-faceted with more defined morphologies than at the O/A ratios of 1.2 and 1.4. At the O/A ratio of 0.6, crystal twinning was evident, as crystals were embedded into each other showing that intergrowth occurred.

As the O/A ratio increased, the edges of the crystals became rounded, especially at the O/A ratio of 1, and the twinning disappeared. During filtration, the precipitate obtained at an O/A ratio of 1.4 formed a multi-layered filter cake, which is shown in Figure 5.3 (e).

From the micrographs, it was evident that the plates became thinner at higher O/A ratios. This means that preferential growth of crystal faces occurred normal/perpendicular to the c-axis when the O/A ratio increased from 0.6 to 1.2. The observed change in morphology can be attributed to either higher supersaturation or enhanced physical interactions between ethanol and the growing $Nd_2(SO_4)_3.8H_2O$ crystals at the higher O/A ratios. However, other methods with high resolution/magnifications could be used to evaluate the changes in morphology at high O/A ratios to gain more insight.

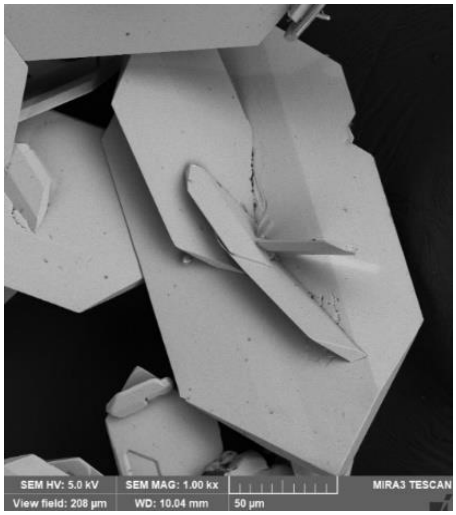

(a)

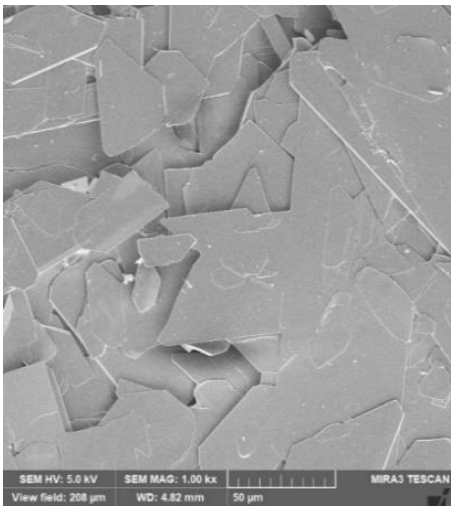

(b)

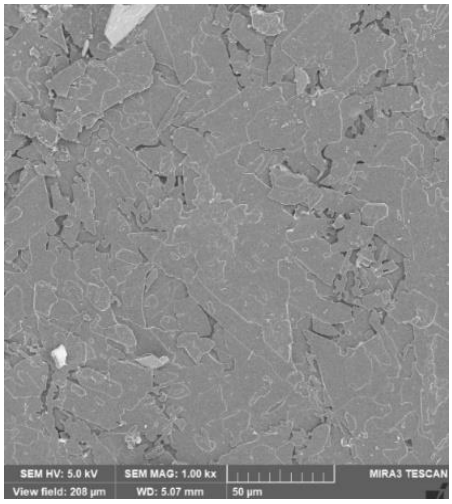

(c)

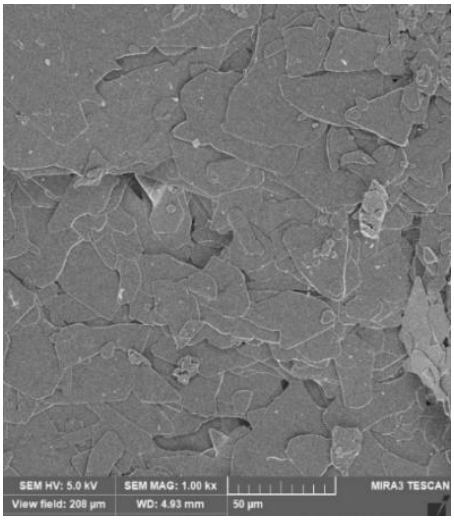

(d)

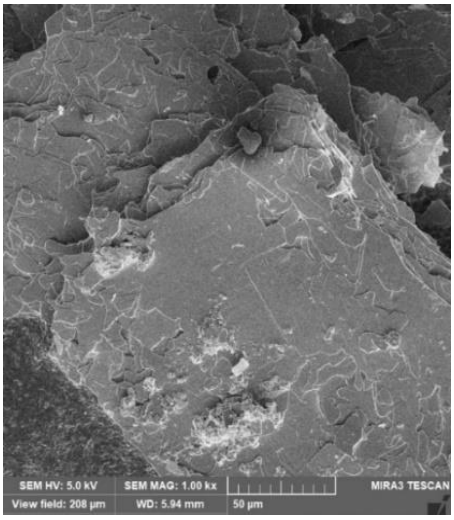

(e)

Figure 5.3: Scaning electrone microscope micrographs of $Nd_2(SO_4)_3.8H_2O$ product. Scale bar 50 µm at organic–to–aqueous ratio: (a) 0.6, (b) 0.8, (c) 1.0, (d) 1.2, and (e) 1.4.

Higher supersaturation increased the nucleation rate and interfacial energies, thereby reducing the growth rate of crystals on other crystal faces at the O/A ratio of 1.4. At higher supersaturations, the crystal surfaces possibly became rough, thereby altering the growth mechanism of the crystals by offering more favorable sites for growth across the crystal surfaces. This possibly led to the transition from layered growth at the lower O/A ratio of 0.6 to rough growth at the O/A ratios of 1.0 and above. The occurrence of kinetic roughening at high or elevated supersaturations and the rounding of edges as the O/A ratio was increased agrees with the findings by Sleutel et al. (2008).

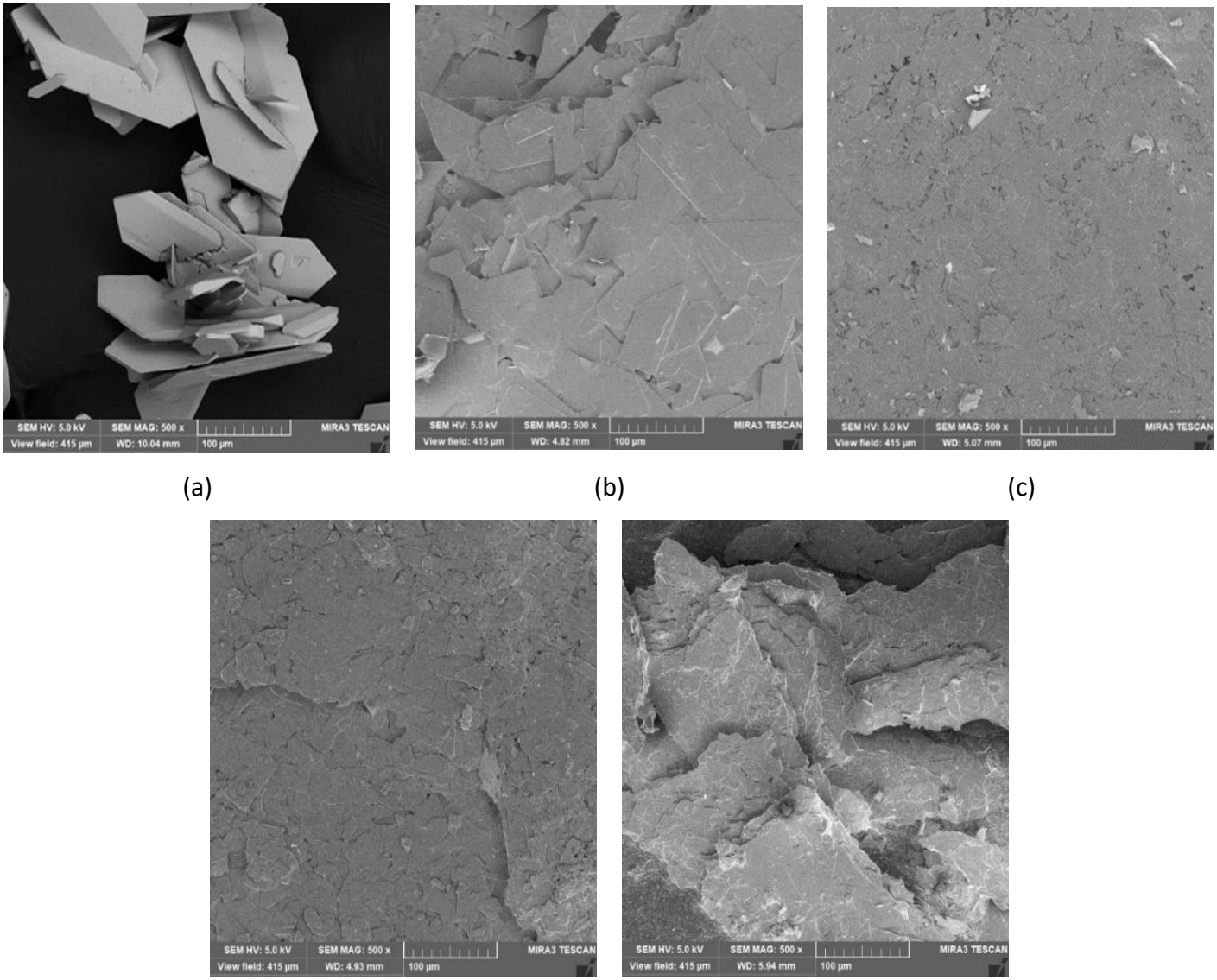

Figure 5.4: Scanning electron microscope micrographs of $Nd_2(SO_4)_3.8H_2O$ product. Scale bar of 100 µm at organic–to–aqueous ratio (a) 0.6, (b) 0.8, (c) 1.0, (d) 1.2, and (e) 1.4.

However, it was not obvious if the change in crystal morphology was solely caused by higher supersaturation. Increasing the amount of ethanol possibly enhanced the interaction between ethanol and the solute molecules, as highlighted by Kumar et al. (2014). There is a possibility that alcohol molecules were adsorbed onto the crystalline surfaces, thereby limiting the solute molecules from accessing kink sites, resulting in slow integration through adsorption (El Bazi et al., 2017; Myerson, 2002).

The hydrogen bonds between the water molecules and ethanol may have inhibited growth from one plane to another (Zhou et al., 2019). Thus, in addition to reducing the solubility of

neodymium sulfate, ethanol possibly acted as an additive that modified the shape of the recovered product at high O/A ratios. Overall, it was observed in this study that increasing the O/A ratio resulted in crystals with different crystal morphology.

5.2.3 Evolution of moments

The evolution of moments was calculated using equations 2.12 and 2.13. A volume shape factor (k_v) of 0.1 and an area shape factor (k_a) of 2.4 were used because the crystals have a plate-like morphology (Mersmann, 2001). A summary of the calculation for the evolution of moments is presented in Appendix A3.

The evolution of normalized zeroth, first, second, and third moments of the PSDs was analysed at the O/A ratios of 0.8 and 1.4 to investigate the cause of the increase in particle size as the O/A ratio increased from 0.8 to 1.4. The zeroth moment (m_0) represents the total number of particles, the first moment (m_1) represents the total particle length, the second moment (m_2) represents the total surface area of particles, and the third moment (m_3) represents the total volume of particles per unit volume of solids-free liquid (Randolph & Larson, 1988).

Figure 5.5 shows that the total number of particles increased significantly between 0.25 h and 0.5 h at the O/A ratio of 0.8. The increase in the total number of particles concurred with a slight increase in the total length of particles at the O/A ratio of 0.8 in the same period. However, the total surface area and total volume remained almost constant. This was probably due to the nucleation of more particles between 0.25 h and 0.5 h. At the O/A ratio of 1.4, the total length remained constant between 0.25 h and 0.5 h as the total number of particles increased while the total surface area and the total volume increased significantly. This is also attributed to the nucleation of more particles within the crystallizer.

The total number of particles, total length, total surface area, and total volume all decreased for the O/A ratio of 0.8 between 0.5 h and 1.0 h. This suggests that redissolution of the product occurred under these conditions. The solution was still supersaturated at this point, so redissolution was potentially an intermediate step of the recrystallization process. However, because the total number of particles decreased, there is a possibility that the recrystallization step was slower than or lagged the dissolution step. The total number of particles decreased only slightly at the O/A ratio of 1.4, while total length, total surface area,

and total volume increased significantly between 0.5 h and 1.0 h. This was due to the particles agglomerating to form bigger particles within the crystallizing system.

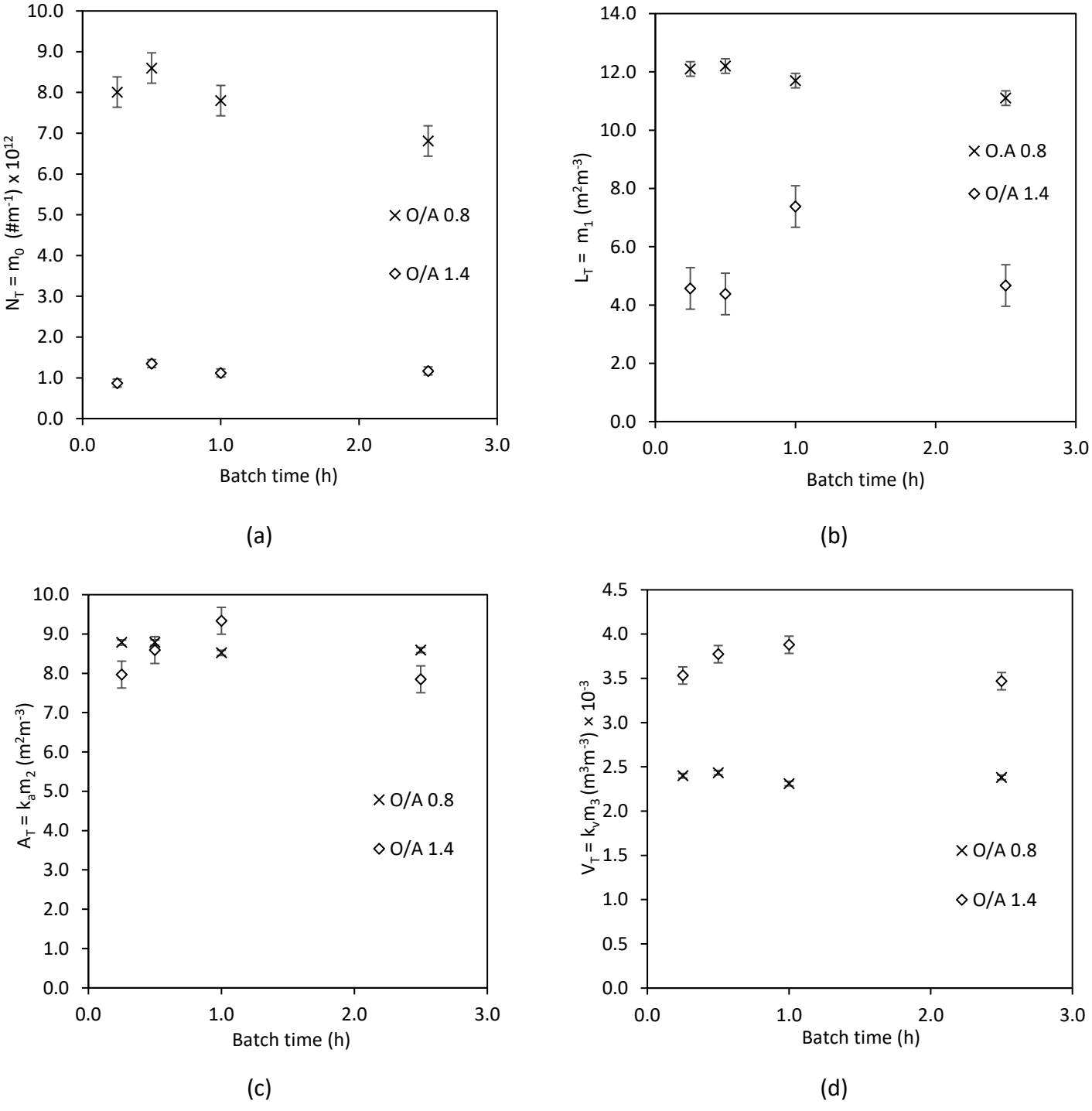

Figure 5.5: Evolution of moments at the organic–to–aqueous ratio of 0.8 and 1.4 (a) Total number (N_T), (b) total length (L_T), (c) total surface area (A_T), (d) total volume (V_T).

Overall, there was a greater number of particles with a higher total length at an O/A ratio of 0.8 than at an O/A ratio of 1.4, with a minimal difference in total surface area between these two O/A ratios. The total volume at an O/A ratio of 1.4 was higher than the total volume at an O/A ratio of 0.8. However, it was expected that the total number of particles for the O/A ratio of 1.4 would be more than for the O/A ratio of 0.8 because of higher supersaturation of the latter leading to a faster nucleation rate, as highlighted by Raj and Kurup (2016).

As noted by Palosaari et al. (2006), the degree of supersaturation is the main parameter that determines the rates of nucleation, crystal growth, and agglomeration. Therefore, it determines the size, morphology, and purity of the crystals. Because the supersaturation at the O/A ratio of 1.4 was higher than at 0.8, a faster nucleation rate was expected at. However, the results show that fewer particles of more volume were obtained at the O/A ratio of 1.4 than at 0.8. This suggests that the smaller particles produced at the O/A of 1.4 possibly agglomerated, resulting in larger mean particle sizes and the PSD curves in Figure 5.2 shifting to the right as the O/A ratio increased. This agrees with observations made by Yu et al. (2006).

To further determine the mechanism of size enlargement that occurred as the O/A ratio was increased, SEM images at different batch times, corresponding to the results presented in Figure 5.5, were obtained. Figure 5.6 is a comparison of the SEM images at different batch times at an O/A ratio of 0.8. The crystals were well-defined and plate-like. There was no evidence of agglomeration as the batch time increased.

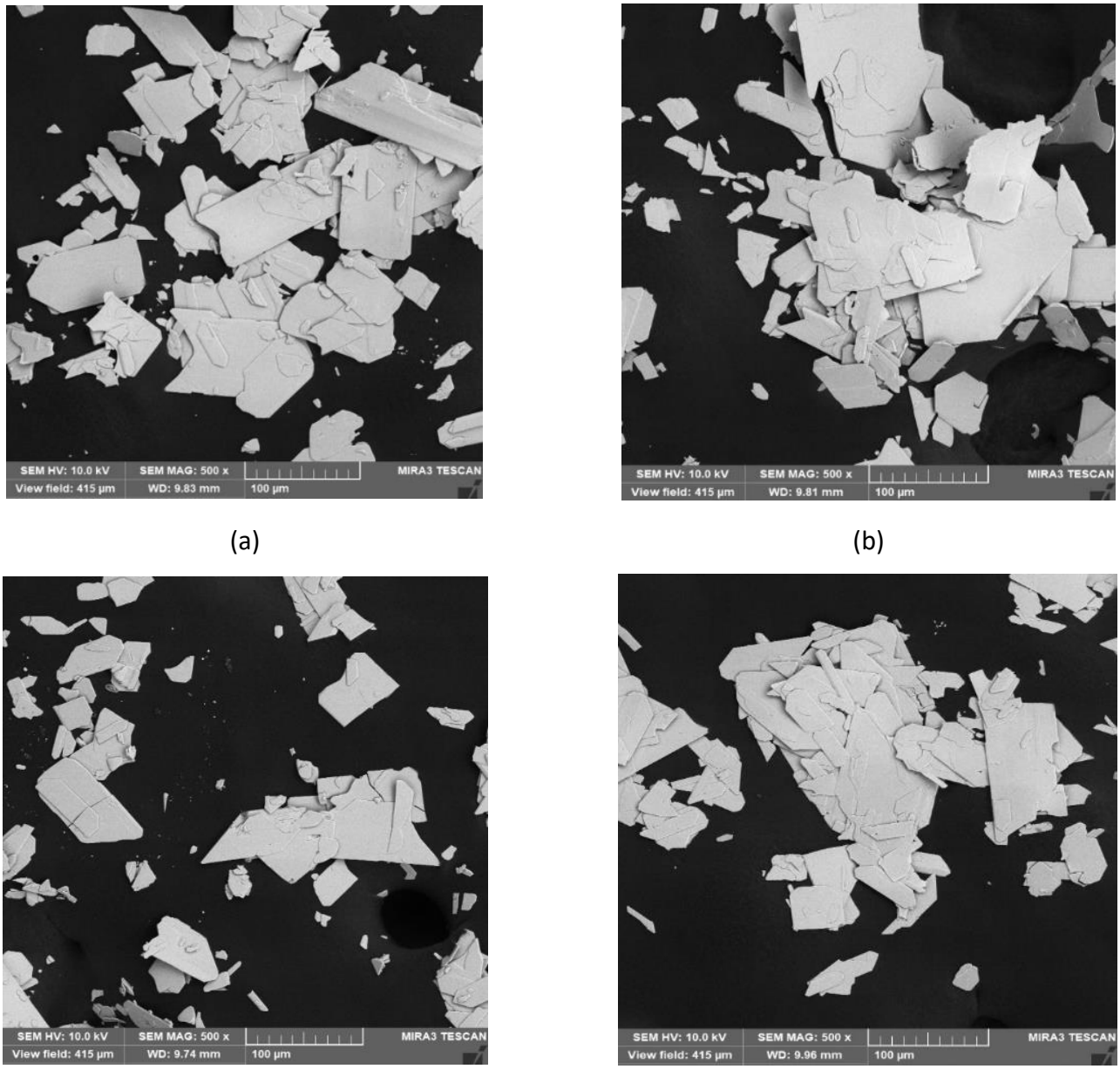

Figure 5.6: Scanning electron microscope micrographs at organic–to–aqueous ratio of 0.8 at different batch times (a) 0.25 h, (b) 0.5 h, (c) 1 h, and (d) 2.5 h.

Figure 5.7 is a comparison of SEM micrographs at different batch times for an O/A ratio of 1.4. It was observed that at all batch times agglomeration was predominant as the images show that the particles are clustered together. This observation supports the conclusions from the evolution of moments that the increase in the particle size at higher O/A ratio was due to agglomeration of the smaller particles.

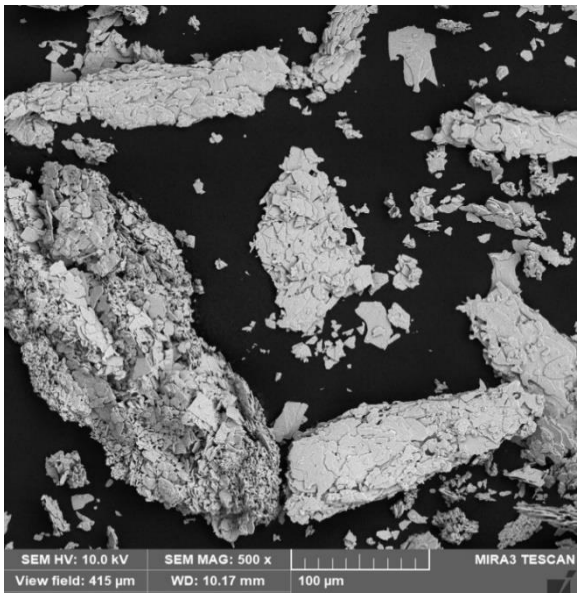

(a)

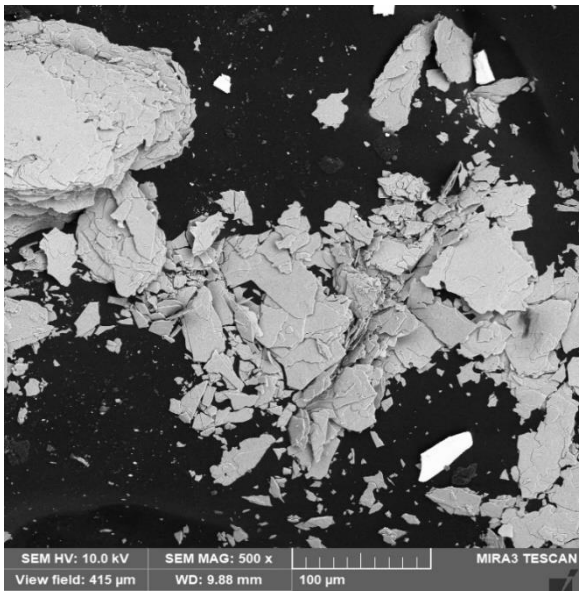

(b)

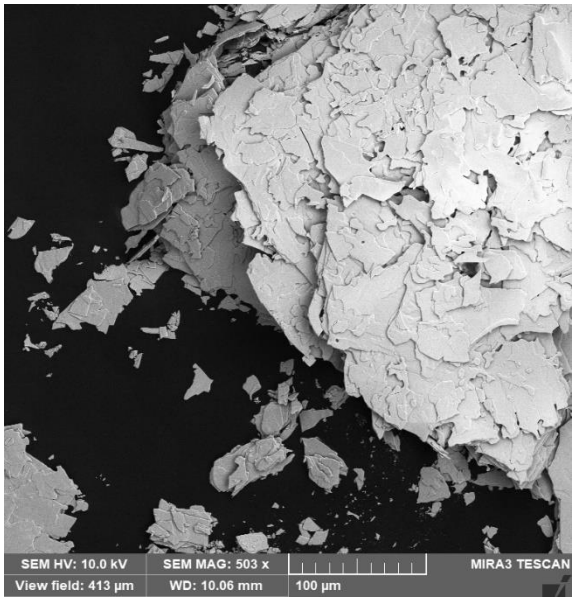

(c)

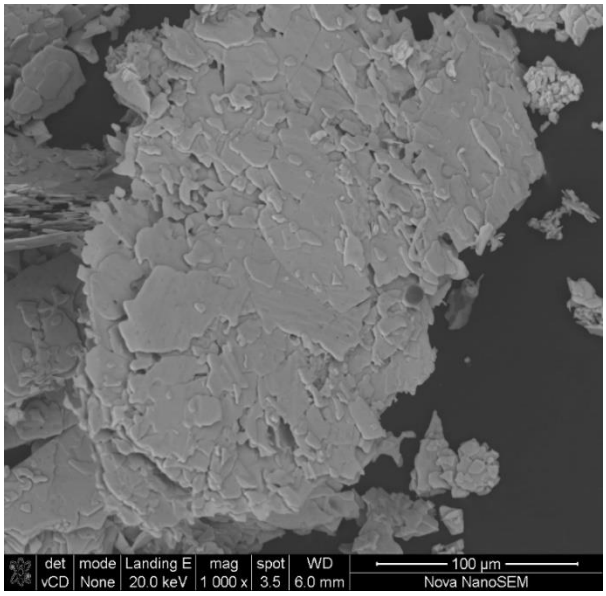

(b)

Figure 5.7: Scanning electron microscope micrographs at organic–to–ratio of 1.4 at different batch times (a) 0.25 h, (b) 0.5 h, (c) 1 h, and (d) 2.5 h.

The PSDs in Figure 5.8 show that the particle size at an O/A ratio of 1.4 was bigger than at an O/A ratio of 0.8 at all batch times.

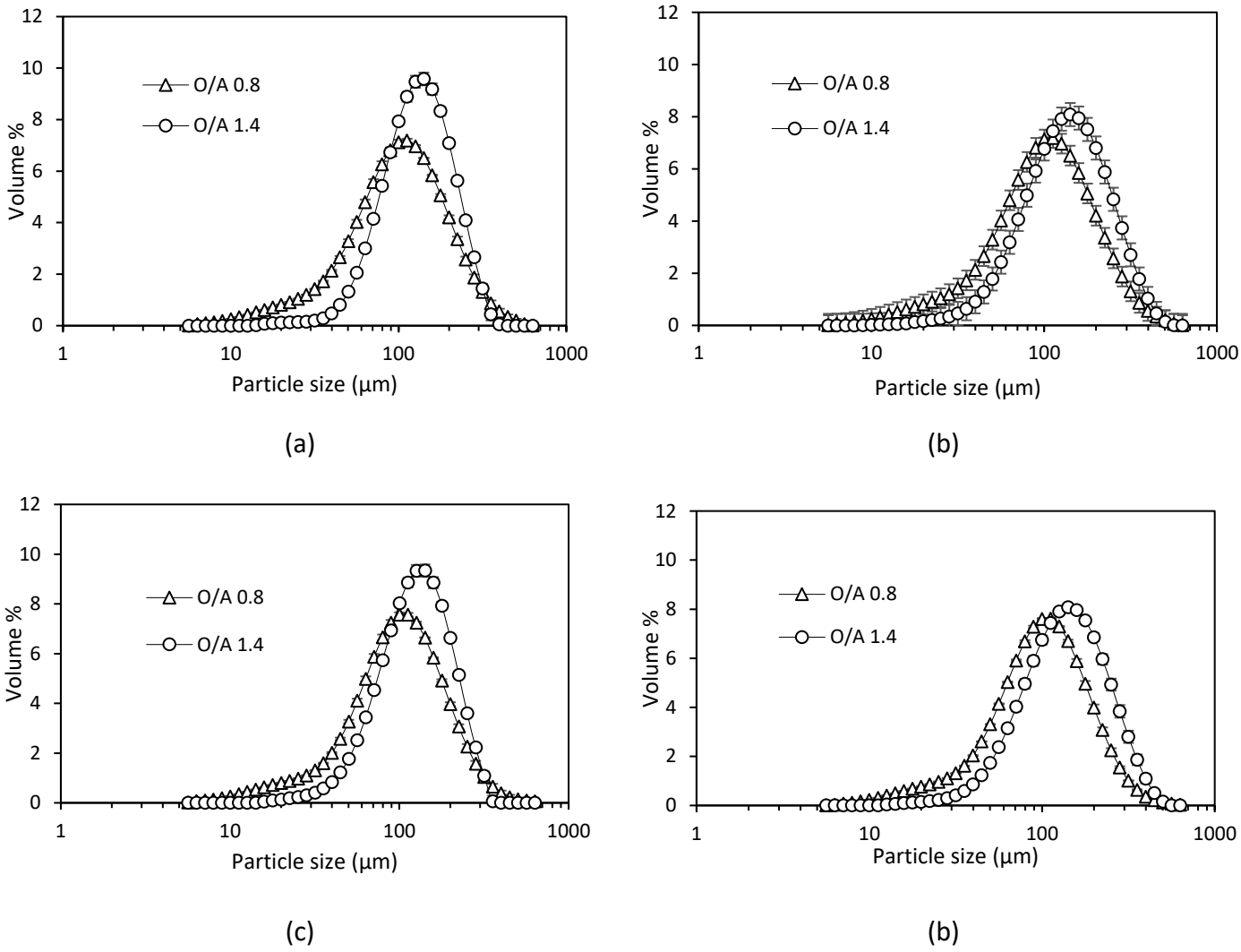

Figure 5.8: Particle size distribution for organic–to–aqueous ratios of 0.8 and 1.4 at different batch times (a) 0.25 h, (b) 0.5 h, (c) 1 h, and (d) 2.5 h.

5.3 Effect of seed loading on quality of $Nd_2(SO_4)_3.8H_2O$ product

The effect of seed loading on the PSD and morphology of $Nd_2(SO_4)_3.8H_2O$ product from the synthetic leach solution was investigated at an O/A ratio of 1.4.

5.3.1 Effect of seed loading on particle size distribution and size of $Nd_2(SO_4)_3.8H_2O$ product

The effect of seed loading on the PSD of $Nd_2(SO_4)_3.8H_2O$ product recovered from the synthetic leach solution was investigated at an O/A ratio of 1.4. The results are shown in Figure 5.9.

The PSD curves shifted to the lower particle size and became narrower as the seed loading (C_S) increased.

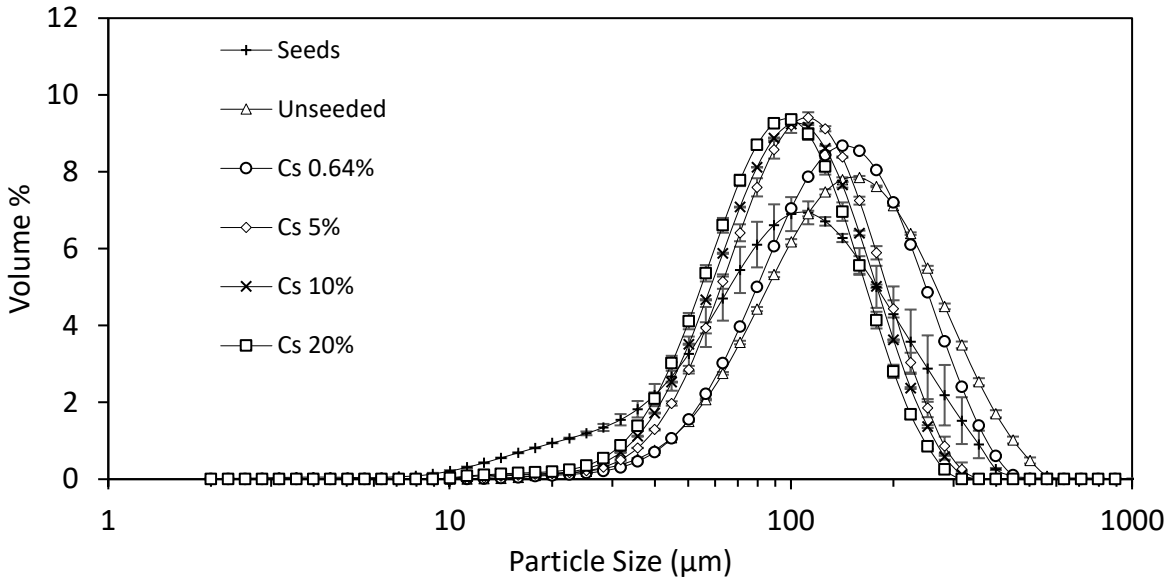

Figure 5.9: Effect of seed loading on particle size distribution of $Nd_2(SO_4)_3.8H_2O$ precipitate produced at organic–to–aqueous ratio of 1.4.

Table **5.2** represents the particle sizes obtained at different seed loadings. It can be noted that the particle sizes decreased as the seed loading was increased, as shown in the PSDs in Figure 5.9.

Table 5.2: Summary of particle sizes of $Nd_2(SO_4)_3.8\ H_2O$ obtained at different seed loading.

Seed Loading	Mean (µm)	Mode (µm)	D_{10} (µm)	D_{50} (µm)	D_{90} (µm)
0	165.8	158.9	63.2	138.1	277.3
0.64	150.0	141.6	63.0	128.8	239.7
5	116	112.5	52.5	100.9	180.1
10	108.8	100.2	48.5	94.1	169.9
20	101.5	100.2	45.7	88.0	157.8

For the unseeded case (0%), uncontrolled primary nucleation occurred but, unexpectedly, produced the biggest particles across the range of seed loadings tested. Because primary nucleation tends to produce smaller particles, the smaller particles formed agglomerates as discussed in Section 5.2.1. Introducing seeds into the crystallizer would promote crystal growth by providing growth sites and sufficient surface area to consume the supersaturation, leading to bigger particles being formed.

It was expected that bigger particles would be produced, and the PSDs would shift to the right when seeding was conducted. However, it is possible that the introduction of seeds inhibited agglomeration and promoted crystal growth. This is one potential reason for the smaller particles obtained in cases where the seed loading was higher than the critical value. The decrease in particle size as the seed loading was increased from 5% to 20% may be attributed to an increase in the number of crystallization sites on which the solute was distributed. This observation agrees with findings by Eder et al. (2011) and Ward et al. (2011).

At seed loadings less than the critical seed loading of 2.98%, the final PSD was almost identical to the final PSD of the unseeded case, as expected. This was because, at seed loading of 0.64%, there were insufficient seeds to provide enough surface area to suppress primary nucleation and provide sufficient surface area for the particles to grow into larger sizes. This behaviour is consistent with findings by Doki et al. (2002).

The width of PSDs is indicated by the span whose value is calculated as follows:

$$\text{Span} = \frac{D_{90} - D_{10}}{D_{50}} \qquad 5.1$$

Where D90 signifies the point in the size distribution, up to and including which, 90% of the total volume of material in the sample is contained. While D50 is the size point below which 50% of the material is contained and D10 is that size below which 10% of the material is contained.

The span of PSDs for seed loadings of 0% and 0.64% were broader than for the cases where the seed loading was above the critical seed loading as shown in Table 5.3. Increasing the seed loading in the antisolvent crystallization of $Nd_2(SO_4)_3$ resulted in particles with narrower PSDs. This agrees with Zhang et al. (2010), Kubota et al. (2001), and Yu et al. (2006), who found that higher seed loadings result in unimodal PSDs as the seeds provide enough surface area to limit the nucleation rate.

Table 5.3: PSD span at different seed loadings.

Seed loading (%)	Span
0	1.54
0.64	1.37
5	1.26
10	1.29
20	1.27

5.3.2 Effect of seed loading on morphology of $Nd_2(SO_4)_3.8H_2O$ product

The morphologies of crystals obtained at different seed loadings were analysed and the micrographs are presented in Figure 5.10. At a seed loading below the critical value, the morphology was the same as for the unseeded system. The morphology was neither well-defined nor distinct. As the seed loading increased, the crystals became flat, well-defined, and plate-like, with rounded edges. At 5% seed loading, the morphology for individual crystals was more distinct, well-defined, and with more rounded edges than at other seed loadings.

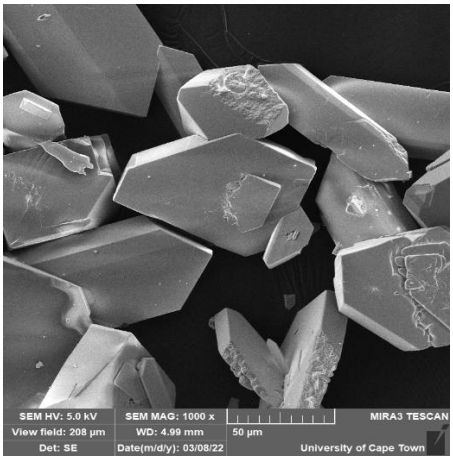

(a)

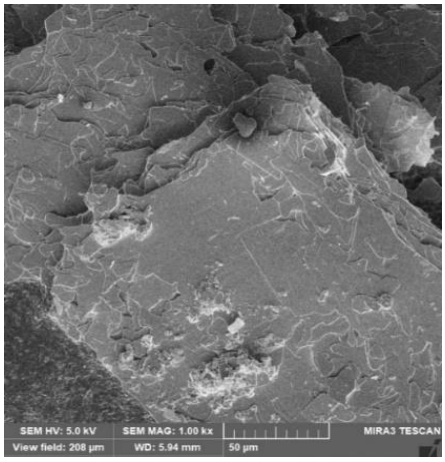

(b)

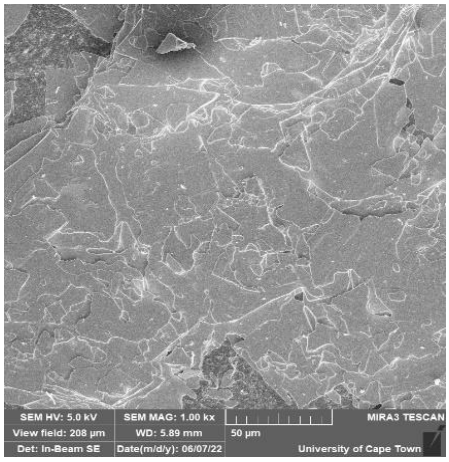

(c)

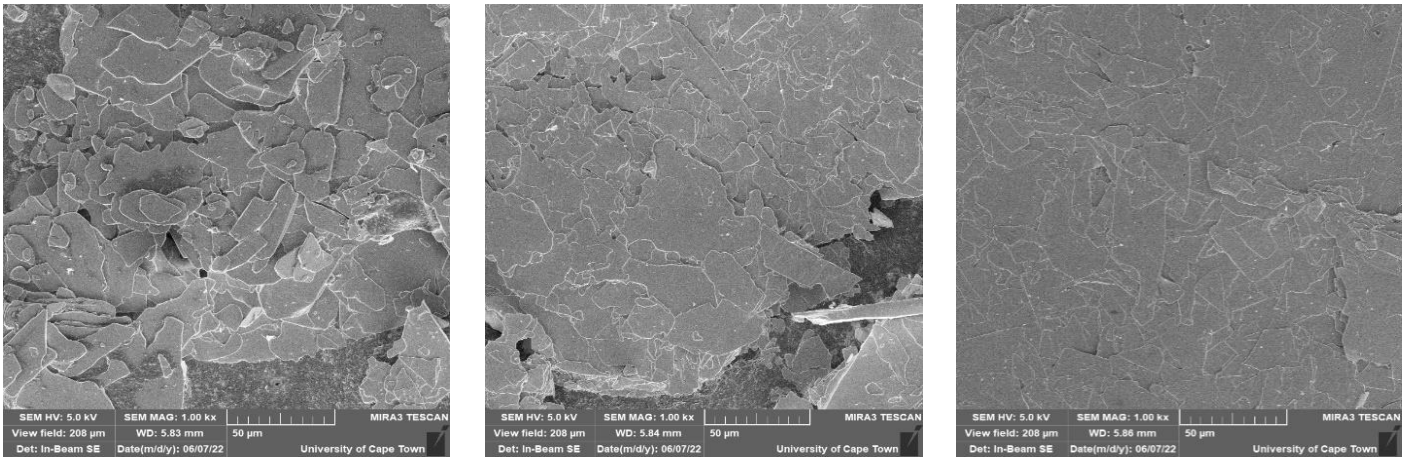

(d) (e) (f)

Figure 5.10: Scanning electron microscope micrographs of $Nd_2(SO_4)_3.8H_2O$ product crystals. Scale bar of 50 µm (a) $Nd_2(SO_4)_3.8H_2O$ seeds, (b) Unseeded, (c) C_S = 0.64 %, (d) C_S = 5%, (e) C_S = 10%, (f) C_S = 20%.

The results show that seed loading above the critical seed loading has an impact on the crystal morphology in antisolvent crystallization of $Nd_2(SO_4)_3.8H_2O$. This was because the seeds provided a surface on which the solute grew into well-faceted crystals. Below the critical seed loading, the seeds were not enough to suppress nucleation and, hence, the crystal morphology was the same as in the unseeded case. At seed loading of 5% (c), there were fewer seeds for the solute to be distributed leading to the growth of individual crystals into well-faceted crystals. Peters et al. (2022) showed that there is an optimal seed loading between 10 and 20%, above which the modal crystal size became smaller due to competition between the rate of generation and consumption of supersaturation. The optimal seed surface area for crystal growth was between 5 and 10%. This agrees with observations in the current study that well-faceted crystals were obtained at a seed loading of 5%, showing that enough seed surface was provided, resulting in distinct crystals with well–defined faces and edges.

The filtration time was reduced by 54 % when the system was seeded at 20% seed loading, while at 5% and 10% seed loading, filtration was reduced by approximately 40%, as shown in Figure 5.11. At the seeding loading of 0.64%, which was below the critical seed loading, the filtration time was almost the same as in the unseeded case.

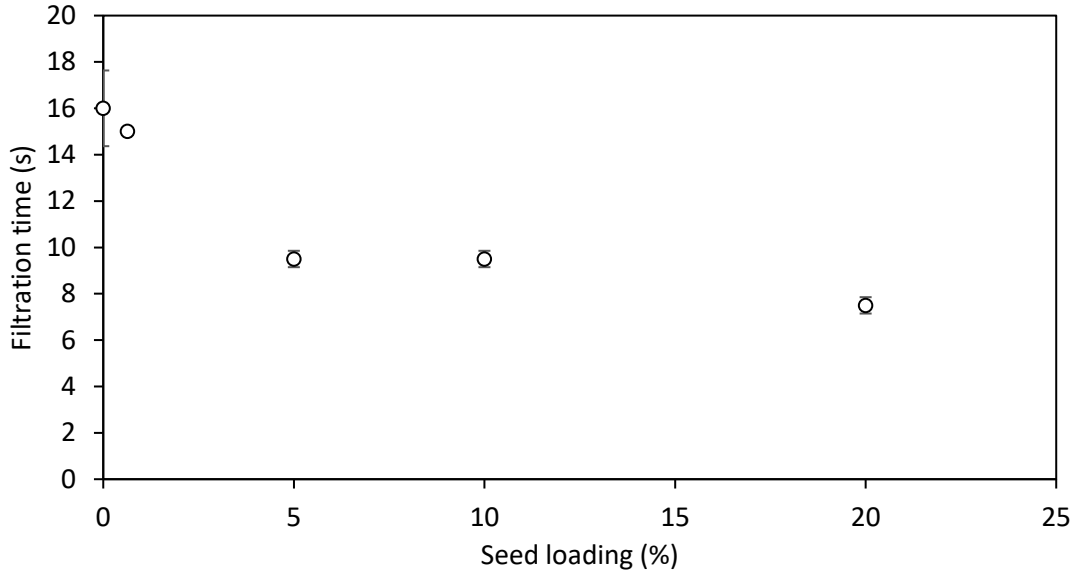

Figure 5.11: Effect of seed loading on filtration time of $Nd_2(SO_4)_3.8H_2O$ product.

The improvement in filtration shows that a narrow PSD and distinct crystals with well–defined morphology of the recovered $Nd_2(SO_4)_3.8H_2O$ product positively influenced the filtration kinetics.

6 Conclusions and Recommendations

6.1 Conclusions

This study aimed to investigate and understand the effect of varying the amount of ethanol (antisolvent) and seed loading on the yield, PSD, and morphology of $Nd_2(SO_4)_3.8H_2O$ product during its recovery from aqueous leach solution, using batch antisolvent crystallization. The leach solution mimicked the concentration of neodymium sulfate in a leach solution from NiMH batteries.

The results showed that increasing the O/A ratio at a batch time of 2.5 h increased both the particle size and yield. Increasing the batch time at an O/A ratio of 0.6 to 24 h improved the yield from 50% to 80%. The increase in yield as the O/A ratio increased was attributed to increased interactions between the antisolvent molecules and the solute, which led to a decrease in the solubility of the solute. The increase in particle size was attributed to agglomeration at higher O/A ratios. At these higher O/A ratios, higher supersaturation caused excessive nucleation and, subsequently, the formation of smaller particles that agglomerated into bigger particles. However, the results show that an increase in the O/A ratio resulted in a change of crystal morphology from well-defined plate-like to layered undefined crystals.

Increasing the seed loading above the critical seed loading of 2.98% resulted in progressively smaller particles of $Nd_2(SO_4)_3.8H_2O$ compared with the unseeded case. However, seeding with $Nd_2(SO_4)_3.8H_2O$ crystals above the critical seed loading produced $Nd_2(SO_4)_3.8H_2O$ crystals with narrower PSDs and improved crystal morphology. Seeding promoted crystal growth and inhibited agglomeration, thus resulting in smaller particles. The seeds also provided enough surface for the solute to grow, resulting in crystals with a well-defined morphology and a narrower PSD. However, even though seeding resulted in smaller particle sizes, there was improved filtration performance compared with the unseeded case. Filtration time was reduced by an average of 47% at seed loadings greater than the critical seed loading. This was attributed to a narrow particle size distribution and distinct crystals with well–defined morphology.

6.2 Recommendations

It is recommended that an actual leach solution from a NiMH battery be used for future studies to gain more insight and increase the chances of industrial implementation of antisolvent crystallization in the recovery of multiple REEs from secondary sources.

To obtain a product that is easier to handle for downstream processes at an industrial scale, an O/A ratio of 0.8 or less must be used and the batch time increased to more than 2.5 h to obtain higher yields. If higher O/A ratios are to be used; it is recommended that seeding be conducted at seed loading higher than the critical seed loading. However, it is recommended that experiments be conducted at an upscaled antisolvent crystallization of neodymium sulfate to obtain the actual mechanisms at an industrial scale.

It will be beneficial to investigate the filterability of $Nd_2(SO_4)_3.8H_2O$ at higher O/A ratios as this influences the final product morphology. Inline measurement of particle size distribution and morphology is also an alternative that can be employed to obtain results in real-time and have a true representation of the mechanisms occurring with the crystallizer at any given timeframe. For future experiments, it is recommended that various seed types with a narrow seed size distribution be used for seeding. It is also recommended that future studies be conducted to determine the surface adsorption/integration mechanisms on seeds in the antisolvent crystallization of REEs.

7 References

Aamir, E., Nagy, Z.K. & Rielly, C.D. 2010. Evaluation of the Effect of Seed Preparation Method on the Product Crystal Size Distribution for Batch Cooling Crystallization Processes. *Crystal Growth & Design.* 10(11):4728-4740. DOI:10.1021/cg100305w.

Adi, H., Larson, I. & Stewart, P. 2007. Use of Milling and Wet Sieving to Produce Narrow Particle Size Distributions of Lactose Monohydrate in the Sub-Sieve Range. *Powder Technology.* 179(1-2):95-99.

Ali, I. & Schneider, P. 2005. Crystallization of Struvite from Metastable Region with Different Types of Seed Crystals. *Journal of Non-Equilibrium Thermodynamics.* 30:95-111. DOI:10.1515/JNETDY.2005.007.

Alonso, E., Wallington, T., Sherman, A., Everson, M., Field, F., Roth, R. & Kirchain, R. 2012. An Assessment of the Rare Earth Element Content of Conventional and Electric Vehicles. *SAE International Journal of Materials and Manufacturing.* 5:473-477. DOI:10.4271/2012-01-1061.

Alves Dias, P., Bobba, S., Carrara, S. & Plazzotta, B. 2020. *The Role of Rare Earth Elements in Wind Energy and Electric Mobility*. Luxembourg: P.o.t.E. Union. Available: https://publications.jrc.ec.europa.eu/repository/handle/JRC122671.

Beckmann, W. 2013. *Crystallization: Basic Concepts and Industrial Applications.* 1. Aufl. Weinheim: Wiley-VCHDOI:10.1002/9783527650323.

Bergfors, T. 2007. Succeeding with Seeding: Some Practical Advice. In *Evolving Methods for Macromolecular Crystallography.* Springer. 1-10.

Borissova, A., Dashova, Z., Lai, X. & Roberts, K.J. 2004. Examination of the Semi-Batch Crystallization of Benzophenone from Saturated Methanol Solution Via Aqueous Antisolvent Drowning-out as Monitored in-Process Using Atr Ftir Spectroscopy. *Crystal Growth & Design.* 4(5):1053-1060. DOI:10.1021/cg049947t.

Charmolue, H. & Rousseau, R.W. 1991. L-Serine Obtained by Methanol Addition in Batch Crystallization. *AIChE Journal.* 37(8):1121-1128. DOI:https://doi.org/10.1002/aic.690370802.

Dhanaraj, G., Byrappa, K., Prasad, V. & Dudley, M. 2010. *Springer Handbook of Crystal Growth.* Springer.

Doki, N., Kubota, N., Sato, A. & Yokota, M. 2001. Effect of Cooling Mode on Product Crystal Size in Seeded Batch Crystallization of Potassium Alum. *Chemical Engineering Journal.* 81(1):313-316. DOI:https://doi.org/10.1016/S1385-8947(00)00172-8.

Doki, N., Kubota, N., Yokota, M. & Chianese, A. 2002. Determination of Critical Seed Loading Ratio for the Production of Crystals of Uni-Modal Size Distribution in Batch Cooling Crystallization of Potassium Alum. *Journal of Chemical Engineering of Japan.* 35(7):670-676. DOI:10.1252/jcej.35.670.

Doki, N., Kayamori, S., Yokota, M., Nemoto, T. & Kato, Y. 2022. Production of Sucrose Crystals of Uni-Modal Size Distribution by Seeded Batch Cooling Crystallization. *Journal of Materials Science and Chemical Engineering.* 10(11):16-23.

Doki, N., Kubota, N., Sato, A., Yokota, M., Hamada, O. & Masumi, F. 1999. Scaleup Experiments on Seeded Batch Cooling Crystallization of Potassium Alum. *AIChE Journal.* 45(12):2527-2533. DOI:https://doi.org/10.1002/aic.690451208.

Eder, R.J.P., Schmitt, E.K., Grill, J., Radl, S., Gruber-Woelfler, H. & Khinast, J.G. 2011. Seed Loading Effects on the Mean Crystal Size of Acetylsalicylic Acid in a Continuous-Flow Crystallization Device. *Crystal Research and Technology.* 46(3):227-237. DOI:https://doi.org/10.1002/crat.201000634.

El Bazi, W., Porte, C., Mabille, I. & Havet, J.-L. 2017. Antisolvent Crystallization: Effect of Ethanol on Batch Crystallization of A Glycine. *Journal of Crystal Growth.* 475:232-238. DOI:https://doi.org/10.1016/j.jcrysgro.2017.06.021.

Ferguson, S., Morris, G., Hao, H., Barrett, M. & Glennon, B. 2013. Characterization of the Anti-Solvent Batch, Plug Flow and Msmpr Crystallization of Benzoic Acid. *Chemical Engineering Science.* 104:44-54. DOI:https://doi.org/10.1016/j.ces.2013.09.006.

Gao, Z., Altimimi, F., Gong, J., Bao, Y., Wang, J. & Rohani, S. 2018. Ultrasonic Irradiation and Seeding to Prevent Metastable Liquid–Liquid Phase Separation and Intensify Crystallization. *Crystal Growth & Design.* 18(4):2628-2635. DOI:10.1021/acs.cgd.8b00284.

Garg, R.K. & Sarkar, D. 2016. Polymorphism Control of P-Aminobenzoic Acid by Isothermal Anti-Solvent Crystallization. *Journal of Crystal Growth.* 454:180-185. DOI:https://doi.org/10.1016/j.jcrysgro.2016.09.023.

Genck, W.J. 2010. Make the Most of Antisolvent Crystallization. *Chemical Processing.* 73(12):21-25.

Granberg, R.A., Bloch, D.G. & Rasmuson, Å.C. 1999. Crystallization of Paracetamol in Acetone–Water Mixtures. *Journal of Crystal Growth.* 198-199:1287-1293. DOI:https://doi.org/10.1016/S0022-0248(98)01013-6.

Gras, M. 2018. Recycling of Metals from Nimh Batteries: Development of Liquid-Liquid Selective Extractions Based on Ionic Liquids. Doctoral dissertation. Université Grenoble Alpes.

Hash, J. & Okorafor, O.C. 2008. Crystal Size Distribution (Csd) of Batch Salting-out Crystallization Process for Sodium Sulfate. *Chemical Engineering and Processing: Process Intensification.* 47(4):622-632. DOI:https://doi.org/10.1016/j.cep.2006.12.006.

He, Y., Gao, Z., Zhang, T., Sun, J., Ma, Y., Tian, N. & Gong, J. 2020. Seeding Techniques and Optimization of Solution Crystallization Processes. *Organic Process Research & Development.* 24(10):1839-1849. DOI:10.1021/acs.oprd.0c00151.

Hojjati, H. & Rohani, S. 2005. Cooling and Seeding Effect on Supersaturation and Final Crystal Size Distribution (Csd) of Ammonium Sulphate in a Batch Crystallizer. *Chemical Engineering and Processing: Process Intensification.* 44(9):949-957. DOI:https://doi.org/10.1016/j.cep.2004.11.003.

Holmbäck, X. & Rasmuson, Å.C. 1999. Size and Morphology of Benzoic Acid Crystals Produced by Drowning-out Crystallisation. *Journal of Crystal Growth.* 198-199:780-788. DOI:https://doi.org/10.1016/S0022-0248(98)01027-6.

IUPAC. 1990. *Nomenclature of Inorganic Chemistry.* 3rd. Blackwell Scientific Publications: Oxford.

Jagadesh, D., Kubota, N., Yokota, M., Sato, A. & Tavare, N.S. 1996. Large and Mono-Sized Product Crystals from Natural Cooling Mode Batch Crystallizer. *Journal of Chemical Engineering of Japan.* 29(5):865-873.

Kakran, M., Sahoo, N.G., Tan, I.L. & Li, L. 2012. Preparation of Nanoparticles of Poorly Water-Soluble Antioxidant Curcumin by Antisolvent Precipitation Methods. *Journal of Nanoparticle Research.* 14(3):757. DOI:10.1007/s11051-012-0757-0.

Kalbasenka, A.N., Spierings, L.C.P., Huesman, A.E.M. & Kramer, H.J.M. 2007. Application of Seeding as a Process Actuator in a Model Predictive Control Framework for Fed-Batch Crystallization of Ammonium Sulphate. *Particle & Particle Systems Characterization.* 24(1):40-48. DOI:https://doi.org/10.1002/ppsc.200601053.

Kaneko, S., Yamagami, Y., Tochihara, H. & Hirasawa, I. 2002. Effect of Supersaturation on Crystal Size and Number of Crystals Produced in Antisolvent Crystallization. *Journal of Chemical Engineering of Japan - J CHEM ENG JPN.* 35:1219-1223. DOI:10.1252/jcej.35.1219.

Kaya, Ş., Peters, E.M., Forsberg, K., Dittrich, C., Stopic, S. & Friedrich, B. 2018. Scandium Recovery from an Ammonium Fluoride Strip Liquor by Anti-Solvent Crystallization. *Metals.* 8(10):767.

Korkmaz, K., Alemrajabi, M., Rasmuson, Å.C. & Forsberg, K.M. 2020. Separation of Valuable Elements from Nimh Battery Leach Liquor Via Antisolvent Precipitation. *Separation and Purification Technology.* 234:115812. DOI:https://doi.org/10.1016/j.seppur.2019.115812.

Kubota, N., Doki, N., Yokota, M. & Sato, A. 2001. Seeding Policy in Batch Cooling Crystallization. *Powder Technology.* 121(1):31-38. DOI:https://doi.org/10.1016/S0032-5910(01)00371-0.

Kumar, R., Siril, P.F. & Soni, P. 2014. Preparation of Nano-Rdx by Evaporation Assisted Solvent Antisolvent Interaction. *Propellants, Explosives, Pyrotechnics.* 39(3):383-389.

Lakerveld, R., Kalbasenka, A., Kramer, H.J., Grievink, J. & Jansens, P.J. Eds. 2007. The Application of Different Seeding Techniques for Solution Crystallization of Ammonium Sulphate. Cape Town, South Africa. 221-228.

Lewis, A., Seckler, M., Kramer, H. & van Rosmalen, G. 2015. *Industrial Crystallization: Fundamentals and Applications.* Cambridge: Cambridge University PressDOI:DOI: 10.1017/CBO9781107280427.

Li, M., Shang, Z. & Hou, B. 2019. Optimizing the Aspect Ratio of Cephalexin in Reactive Crystallization by Controlling Supersaturation and Seeding Policy. *Transactions of Tianjin University.* 25(4):348-356. DOI:10.1007/s12209-019-00185-z.

Loï Mi Lung-Somarriba, B., Moscosa-Santillan, M., Porte, C. & Delacroix, A. 2004. Effect of Seeded Surface Area on Crystal Size Distribution in Glycine Batch Cooling Crystallization: A Seeding Methodology. *Journal of Crystal Growth.* 270(3):624-632. DOI:https://doi.org/10.1016/j.jcrysgro.2004.07.015.

Lovette, M.A., Browning, A.R., Griffin, D.W., Sizemore, J.P., Snyder, R.C. & Doherty, M.F. 2008. Crystal Shape Engineering. *Industrial & Engineering Chemistry Research.* 47(24):9812-9833. DOI:10.1021/ie800900f.

Lucas, J., Lucas, P., Le Mercier, T., Rollat, A. & Davenport, W.G. 2014. *Rare Earths: Science, Technology, Production and Use.* Elsevier.

Ma, Y., Svärd, M., Xiao, X., Gardner, J.M., Olsson, R.T. & Forsberg, K. 2020. Precipitation and Crystallization Used in the Production of Metal Salts for Li-Ion Battery Materials: A Review. *Metals.* 10(12):1609. Available: https://www.mdpi.com/2075-4701/10/12/1609.

Mersmann, A. 2001. *Crystallization Technology Handbook.* Second. New York: Marcel Dekker. MordorIntelligence. 2022. *Rare Earth Elements Market - Growth, Trends, Covid 19 Impact and Forecasts (2022 - 2027)*. Hyderabad, Telangana.

Mullin, J.W. 2001. *Crystallization.* Oxford: Butterworth Heinemann.Fourth Edition.

Myerson, A. 2002. *Handbook of Industrial Crystallization.* 2nd. Butterworth-Heinemann.

Myerson, A., Erdemir, D. & Lee, A.Y. 2019. *Handbook of Industrial Crystallization.* 3rd. Cambridge: Cambridge University PressDOI:DOI: 10.1017/9781139026949.

Norouzi, M., Tahernejad, M., Ghorban Hosseini, S. & Tavangar, S. 2020. Taguchi Optimization of Solvent-Antisolvent Crystallization to Prepare Ammonium Perchlorate Particles. *Chemical Engineering & Technology.* 43(11):2215-2223. DOI:https://doi.org/10.1002/ceat.202000180.

Nowee, S.M., Abbas, A. & Romagnoli, J.A. 2008. Model-Based Optimal Strategies for Controlling Particle Size in Antisolvent Crystallization Operations. *Crystal Growth & Design.* 8(8):2698-2706. DOI:10.1021/cg700720t.

Nyvlt, J. 1984. *Kinetics of Industrial Crystallization.* Elsevier Science Pub. Co., Inc.[distributor].

O'Grady, D., Barrett, M., Casey, E. & Glennon, B. 2007. The Effect of Mixing on the Metastable Zone Width and Nucleation Kinetics in the Anti-Solvent Crystallization of Benzoic Acid. *Chemical Engineering Research and Design.* 85(7):945-952. DOI:https://doi.org/10.1205/cherd06207.

OLI-Systems-Inc. 2022. *Oli Studio 11.0 Morris*. Available: https://www.olisystems.com/ [Available: https://www.olisystems.com/].

Palosaari, S., Louhi-Kultanen, M. & Sha, Z. 2006. Industrial Crystallization. *Handbook of Industrial Drying, Fourth Edition.* 10.1201/9781420017618.ch51. DOI:10.1201/9781420017618.ch51.

Parambil, J. & Heng, J. 2017. Seeding in Crystallisation. In *Nato Science for Peace and Security Series A: Chemistry and Biology.* Springer Science. 235-245. DOI:10.1007/978-94-024-1117-1_13.

Peters, E.M., Svärd, M. & Forsberg, K. 2022. Impact of Process Parameters on Product Size and Morphology in Hydrometallurgical Antisolvent Crystallization. *CrystEngComm.* 24(15):2851-2866. DOI:10.1039/D2CE00050D.

Peters, E.M., Kaya, Ş., Dittrich, C. & Forsberg, K. 2019. Recovery of Scandium by Crystallization Techniques. *Journal of Sustainable Metallurgy.* 5(1):48-56. DOI:10.1007/s40831-019-00210-4.

Raj, R., Arun & Kurup, M. 2016. Antisolvent Crystallization: A Novel Approach to Bioavailability Enhancement. *European Journal of Biomedical and Pharmaceutical Sciences.* 3:230-234.

Randolph, A.D. & Larson, M.A. 1988. *Theory of Particulate Processes: Analysis and Techniques of Continuous Crystallization.* 2nd. San Diego: Academic Press.

Regy, S., Mangin, D., Klein, J.P. & Lieto, J. Eds. 2002. Phosphate Recovery by Stuvite Precipitation in a Stirred Reactor. Centre Europeen d'Etudes des Polyphosphates (CEEP).

Sleutel, M., Maes, D., Wyns, L. & Willaert, R. 2008. Kinetic Roughening of Glucose Isomerase Crystals. *Crystal Growth & Design.* 8(12):4409-4414. DOI:10.1021/cg701220t.

Takiyama, H., Otsuhata, T. & Matsuoka, M. 1998. Morphology of Nacl Crystals in Drowning-out Precipitation Operation. *Chemical Engineering Research and Design.* 76(7):809-814. DOI:https://doi.org/10.1205/026387698525559.

Ulrich, J. & Jones, M. 2006. Heat and Mass Transfer Operations—Crystallization. *Chemical Engineering and Chemical Process Technology.* 2.

Vedantam, S. & Ranade, V.V. 2013. Crystallization: Key Thermodynamic, Kinetic and Hydrodynamic Aspects. *Sadhana.* 38(6):1287-1337. DOI:10.1007/s12046-013-0195-4.

Vorobei, A.M., Pokrovskiy, O.I., Ustinovich, K.B., Krotova, L.I., Parenago, O.O. & Lunin, V.V. 2016. Effect of Solvent Type and Concentration on Size and Morphology of Arbidol Microparticles Obtained by Supercritical Antisolvent Precipitation. *Russian Journal of Physical Chemistry B.* 10(7):1072-1077. DOI:10.1134/S1990793116070198.

Wang, H.-Y. & Ward, J.D. 2015. Seeding and Optimization of Batch Reactive Crystallization. *Industrial & Engineering Chemistry Research.* 54(38):9360-9368. DOI:10.1021/acs.iecr.5b00185.

Wang, J., Burken, J.G. & Zhang, X. 2006. Effect of Seeding Materials and Mixing Strength on Struvite Precipitation. *Water Environment Research.* 78(2):125-132. Available: http://www.jstor.org.ezproxy.uct.ac.za/stable/25045953 [2022/09/14/].

Ward, J.D., Yu, C.-C. & Doherty, M.F. 2011. A New Framework and a Simpler Method for the Development of Batch Crystallization Recipes. *AIChE Journal.* 57(3):606-617. DOI:https://doi.org/10.1002/aic.12284.

Warstat, A. & Ulrich, J. 2006. Seeding During Batch Cooling Crystallization – an Initial Approach to Heuristic Rules. *Chemical Engineering & Technology.* 29(2):187-190. DOI:https://doi.org/10.1002/ceat.200500372.

Waval, A.S., Patel, P., Nemade, P.R. & Mathpati, C.S. 2020. Experimental Studies in Antisolvent Crystallization: Effect of Antisolvent Ratio and Mixing Patterns. *Indian Journal of Chemical Technology.* 27(1):18-25.

Xu, D., Xue, D. & Ratajczak, H. 2005. Morphology and Structure Studies of Kdp and Adp Crystallites in the Water and Ethanol Solutions. *Journal of Molecular Structure.* 740(1):37-45. DOI:https://doi.org/10.1016/j.molstruc.2005.01.016.

Yazdanpanah, N. & Nagy, Z.K. 2020. *The Handbook of Continuous Crystallization.* Royal Society of Chemistry.

Yoon, H.-S., Kim, C.-J., Chung, K.W., Lee, J.-Y., Shin, S.M., Lee, S.-J., Joe, A.R., Lee, S.-I. et al. 2014. Leaching Kinetics of Neodymium in Sulfuric Acid of Rare Earth Elements (Ree) Slag Concentrated by Pyrometallurgy from Magnetite Ore. *Korean Journal of Chemical Engineering.* 31(10):1766-1772. DOI:10.1007/s11814-014-0078-3.

Yu, Z.Q., Tan, R.B.H. & Chow, P.S. 2005. Effects of Operating Conditions on Agglomeration and Habit of Paracetamol Crystals in Anti-Solvent Crystallization. *Journal of Crystal Growth.* 279(3):477-488. DOI:https://doi.org/10.1016/j.jcrysgro.2005.02.050.

Yu, Z.Q., Chow, P.S. & Tan, R.B.H. 2006. Seeding and Constant-Supersaturation Control by Atr-Ftir in Anti-Solvent Crystallization. *Organic Process Research & Development.* 10(4):717-722. DOI:10.1021/op060058j.

Zhang, C.-t., Wang, H.-r. & Wang, Y.-l. 2010. Internally Generated Seeding Policy in Anti-Solvent Crystallization of Ceftriaxone Sodium. *Chemical Engineering and Processing: Process Intensification.* 49(4):396-401. DOI:https://doi.org/10.1016/j.cep.2010.03.001.

Zhang, F., Shan, B., Wang, Y., Zhu, Z., Yu, Z.-Q. & Ma, C.Y. 2021. Progress and Opportunities for Utilizing Seeding Techniques in Crystallization Processes. *Organic Process Research & Development.* 25(7):1496-1511. DOI:10.1021/acs.oprd.1c00103.

Zhang, Y., Jiang, Y., Zhang, D., Qian, Y. & Wang, X.Z. 2015. Metastable Zone Width, Crystal Nucleation and Growth Kinetics Measurement in Anti-Solvent Crystallization of B-Artemether in the Mixture of Ethanol and Water. *Chemical Engineering Research and Design.* 95:187-194. DOI:https://doi.org/10.1016/j.cherd.2014.10.018.

Zhao, L., Li, J., He, J., Luo, P., Shi, L., Zhou, J. & Pang, A. 2020. A Study of Solvent and Antisolvent Influence on the Crystal Morphology of ϵ-Cl-20 by a Modified Attachment Energy Model. *Propellants, Explosives, Pyrotechnics.* 45(7):1117-1128. DOI:https://doi.org/10.1002/prep.201900386.

Zhao, X., Song, K., Wang, S., Zu, Y., Li, N. & Yu, X. 2013. Micronization of the Pharmaceutically Active Agent Genipin by an Antisolvent Precipitation Process. *Chemical Engineering & Technology.* 36(1):33-42. DOI:https://doi.org/10.1002/ceat.201200036.

Zhou, X., Shan, J., Chen, D. & Li, H. 2019. Tuning the Crystal Habits of Organic Explosives by Antisolvent Crystallization: The Case Study of 2,6-Dimaino-3,5-Dinitropyrazine-1-Oxid (Llm-105). *Crystals.* 9(8):392. DOI:10.3390/cryst9080392.

8 Appendix

A1 Seed surface area calculations

The calculations were conducted using equation 3.1.

$$S_a = \frac{W_S\, k_a}{\rho k_v L_S}$$

A volume shape factor (k_v) of 0.01 and surface shape factor (k_a) of 2.4 were used as the seed crystals morphology was plate-like (Mersmann, 2001). From Section 4.4, the seed mean size (L_S) was 117.2 µm. The density of the neodymium particles obtained from OLI Stream Analyser was 2.850 g/cm^3. The table presents the seed mass used in the experiments for each seed loading.

Table 8.1: Seed mass used for the seed loading experiments.

Seed loading (%)	W_S [Seed mass (g)]	Seed surface area (cm^2)
0.64	0.0026	18.7
5	0.0217	156
10	0.0426	306
20	0.0833	597

For example, calculation at 0.64% seed loading the seed surface area was calculated as:

$$S_a = \frac{0.0026\ \text{g} \times 2.4}{2.85\ \text{g/cm}^3 \times 0.01 \times 0.0117\ \text{cm}}$$

$$= 18.7\ \text{cm}^2$$

A2 Supersaturation calculation

Table 8.2: Data from OLI Stream Analyser.

O/A ratio	Activity coefficient (SO_4^{2-})	Activity coefficient (Nd^{+3})	Solubility of $Nd_2(SO_4)_3.8H_2O$	$[Nd^{3+}]$	$[SO_4^{2-}]$	Ksp	Supersaturation
0.0	0.617	0.304	0.00607	0.0121	0.0182	8.89×10^{-10}	1.93×10^{-2}
0.6	62.9	1.45	0.00354	0.00709	0.0106	6.07×10^{-11}	5.20×10^{5}
0.8	202	2.06	0.00311	0.00621	0.00932	3.12×10^{-11}	3.55×10^{7}
1.0	560	2.66	0.00276	0.00552	0.00823	1.73×10^{-11}	1.24×10^{9}
1.2	1375	3.24	0.00248	0.00496	0.00744	1.02×10^{-11}	2.72×10^{10}
1.4	**3068**	**3.83**	**0.00225**	**0.00451**	**0.00676**	**6.27×10^{-12}**	**4.23×10^{11}**

*The numbers highlighted in bold are used in the calculations.

$[Nd^{3+}]$ = 2 × solubility of $Nd_2(SO_4)_3.8H_2O$

= 2 × 0.00225

= 0.00451 mol

$[SO_4^{2-}]$ = 3 × solubility of $Nd_2(SO_4)_3.8H_20$

= 3 × 0.00225

= 0.00676 mol

Ksp = $[Nd^{3+}]^2 \times [SO_4^{2-}]^3$

= $(0.00225)^3 \times (0.00676)^2$

= 6.27×10^{-12} mol^5

Supersaturation $S = \frac{\Pi(\gamma_i C_i)^{\upsilon_i}}{K_{sp}}$

$$= \frac{(3068 \times 0.00676)^3 \, (3.83 \times 0.00451)^2}{6.27 \times 10^{-12}}$$

= 4.23×10^{11}

A3 Evolution of moments calculations

The PSD was measured using laser diffraction and an average of three runs was done per experiment. The target obscuration was 12 ± 0.5%, with a weighted residual of less than 1%. Figure 8.1 shows the report from the laser diffraction.

MASTERSIZER 2000

Result Analysis Report

Sample Name: OA 1.4 2nd Run 4.03995 g per L - Average	**SOP Name:** Neodynium sulfate R1_Jonathan	**Measured:** Friday, May 20, 2022 2:46:21 PM	
Sample Source & type: Paris	**Measured by:** Alab	**Analysed:** Friday, May 20, 2022 2:46:22 PM	
Sample bulk lot ref: 123-ABC	**Result Source:** Averaged		
Particle Name: Neodynium sulfate R1	**Accessory Name:** Hydro 2000SM (A)	**Analysis model:** General purpose	**Sensitivity:** Enhanced
Particle RI: 1.333	**Absorption:** 0.1	**Size range:** 0.020 to 2000.000 um	**Obscuration:** 12.21 %
Dispersant Name: Water + ethanol	**Dispersant RI:** 1.345	**Weighted Residual:** 0.402 %	**Result Emulation:** Off
Concentration: 0.2080 %Vol	**Span :** 1.538	**Uniformity:** 0.476	**Result units:** Volume
Specific Surface Area: 0.0529 m²/g	**Surface Weighted Mean D[3,2]:** 113.314 um	**Vol. Weighted Mean D[4,3]:** 156.644 um	

d(0.1): 63.849 um **d(0.5):** 138.372 um **d(0.9):** 276.735 um

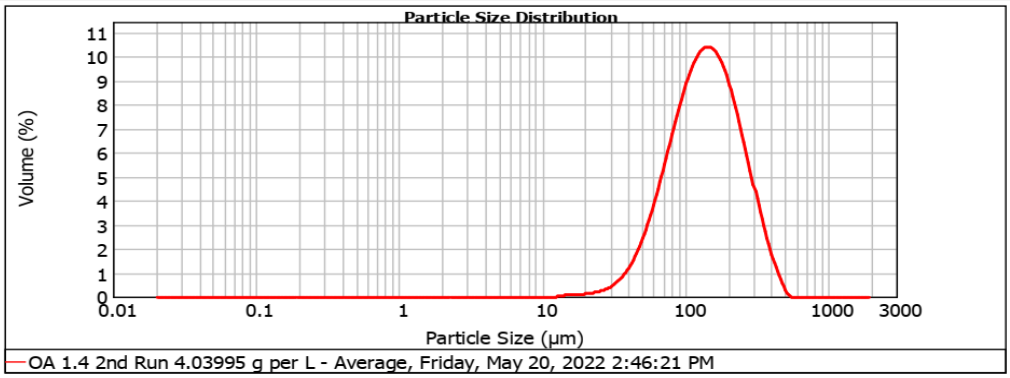

Size (µm)	Volume In %	Size (µm)	Volume In %	Size (µm)	Volume In %	Size (µm)	Volume In %	Size (µm)	Volume In %	Size (µm)	Volume In %
0.020	0.00	0.142	0.00	1.002	0.00	7.096	0.00	50.238	2.13	355.656	1.69
0.022	0.00	0.159	0.00	1.125	0.00	7.962	0.00	56.368	2.83	399.052	0.98
0.025	0.00	0.178	0.00	1.262	0.00	8.934	0.00	63.246	3.64	447.744	0.43
0.028	0.00	0.200	0.00	1.416	0.00	10.024	0.00	70.963	4.50	502.377	0.02
0.032	0.00	0.224	0.00	1.589	0.00	11.247	0.00	79.621	5.38	563.677	0.00
0.036	0.00	0.252	0.00	1.783	0.00	12.619	0.01	89.337	6.20	632.456	0.00
0.040	0.00	0.283	0.00	2.000	0.00	14.159	0.06	100.237	6.91	709.627	0.00
0.045	0.00	0.317	0.00	2.244	0.00	15.887	0.06	112.468	7.44	796.214	0.00
0.050	0.00	0.356	0.00	2.518	0.00	17.825	0.08	126.191	7.75	893.367	0.00
0.056	0.00	0.399	0.00	2.825	0.00	20.000	0.10	141.589	7.81	1002.374	0.00
0.063	0.00	0.448	0.00	3.170	0.00	22.440	0.14	158.866	7.61	1124.683	0.00
0.071	0.00	0.502	0.00	3.557	0.00	25.179	0.20	178.250	7.15	1261.915	0.00
0.080	0.00	0.564	0.00	3.991	0.00	28.251	0.31	200.000	6.45	1415.892	0.00
0.089	0.00	0.632	0.00	4.477	0.00	31.698	0.47	224.404	5.58	1588.656	0.00
0.100	0.00	0.710	0.00	5.024	0.00	35.566	0.72	251.785	4.59	1782.502	0.00
0.112	0.00	0.796	0.00	5.637	0.00	39.905	1.08	282.508	3.57	2000.000	
0.126	0.00	0.893	0.00	6.325	0.00	44.774	1.54	316.979	2.57		
0.142	0.00	1.002	0.00	7.096	0.00	50.238		355.656			

Operator notes:

Figure 8.1: Laser diffraction report.

Method of moments was used on an MS Excel spreadsheet using data from the laser diffraction (Mastersizer 2000) report.

Table 8.3: Calculation of evolution of moments.

Particle size (µm)	Delta L (m)	lbar (m)	Volume (%)	Number
7.96				
8.93	9.72E−07	8.45E−06	0	0.00E+00
10.0	1.09E−06	9.48E−06	0	0.00E+00
11.2	1.22E−06	1.06E−05	0	0.00E+00
12.6	1.37E−06	1.19E−05	0	0.00E+00
14.2	**1.54E−06**	**1.34E−05**	**0.0141**	**2.33E+10**
15.9	**1.73E−06**	**1.50E−05**	**0.0576**	**6.74E+10**
17.8	1.94E−06	1.69E−05	0.0630	5.22E+10
20.0	2.17E−06	1.89E−05	0.0773	4.54E+10
22.4	2.44E−06	2.12E−05	0.0976	4.06E+10
25.2	2.74E−06	2.38E−05	0.135	3.99E+10
28.3	3.07E−06	2.67E−05	0.199	4.15E+10
31.7	3.45E−06	3.00E−05	0.306	4.51E+10
35.6	3.87E−06	3.36E−05	0.474	4.95E+10
39.9	4.34E−06	3.77E−05	0.723	5.34E+10
44.8	4.87E−06	4.23E−05	1.08	5.63E+10
50.2	5.46E−06	4.75E−05	1.54	5.70E+10
56.4	6.13E−06	5.33E−05	2.13	5.60E+10
63.2	6.88E−06	5.98E−05	2.83444	5.26E+10
71.0	7.72E−06	6.71E−05	3.64	4.79E+10
79.6	8.66E−06	7.53E−05	4.50	4.19E+10
89.3	9.72E−06	8.45E−05	5.38	3.54E+10
100	1.09E−05	9.48E−05	6.20	2.89E+10
112	1.22E−05	1.06E−04	6.91	2.28E+10
126	1.37E−05	1.19E−04	7.44	1.74E+10
142	1.54E−05	1.34E−04	7.75	1.28E+10
159	1.73E−05	1.50E−04	7.81	9.15E+09
178	1.94E−05	1.69E−04	7.61	6.31E+09
200	2.17E−05	1.89E−04	7.15	4.20E+09

224	2.44E−05	2.12E−04	6.45	2.68E+09
252	2.74E−05	2.38E−04	5.58	1.64E+09
283	3.07E−05	2.67E−04	4.56	9.55E+08
317	3.45E−05	3.00E−04	3.57	5.26E+08
356	3.87E−05	3.36E−04	2.57	2.68E+08
399	4.34E−05	3.77E−04	1.69	1.25E+08
448	4.87E−05	4.23E−04	0.979	5.12E+07
502	5.46E−05	4.75E−04	0.430	1.59E+07
564	6.13E−05	5.33E−04	0.016	4.28E+05
		Zeroth moment	**m_0**	**9.13E+11**
		First moment	**m_1**	**4.53E+07**
		Second moment	**m_2**	**3499**
		Third moment	**m_3**	**0.397**
		Fourth moment	**m_4**	**0.0000623**

*The numbers highlighted in bold are used in the calculations.

$$\text{Delta L} = \frac{15.9 - 14.2}{1\,000\,000}$$

$$= 1.73 \times 10^{-6}$$

$$\bar{L} = 14.2 \times 10^{-6} + \frac{\text{Delta L}}{2}$$

$$= (14.2 + \frac{1.73}{2}) \times 10^{-6}$$

$$= 1.50 \times 10^{-5}$$

The number of particles is calculated using the following equation.

$$N = \frac{\text{Vol \%}_i \times \text{Conc (vol\%)}}{100} \times \frac{1}{k_v \bar{L}^3}$$

Where: N is the number of particles in a size range.

vol% is the volume of the solids in a size range (measured by the instrument).

conc. (vol%) is the total concentration of solids (vol%) (measured by the instrument).

K_V is the volume shape factor ($\pi/6$).

The conversion to moments was calculated as:

m_0 = sum (N)

m_1 = sum ($\bar{L} \times N$)

m_2 = sum ($\bar{L}^2 \times N$)

m_3 = sum ($\bar{L}^3 \times N$)

m_4 = sum ($\bar{L}^3 \times N$)

The ratio of these moments gives the surface-weighted mean (m_3 to m_2) and the volume-weighted mean averages (m_4 to m_3).

$$D_{3,2} = \frac{m_3}{m_2} = \frac{0.397}{34985} = 1.14 \times 10^{-4} \text{ m} = 113.6 \text{ µm}$$

$$D_{4,3} = \frac{m_4}{m_3} = \frac{0.0000623}{0.397} = 1.57 \times 10^{-4} \text{ m} = 156.8 \text{ µm}$$